

2D reactive transport modeling; Dávila et al. (2016)

1 **2D reactive transport modeling of the interaction between a marl and a**  
2 **CO<sub>2</sub>-rich sulfate solution under supercritical CO<sub>2</sub> conditions**

3 Gabriela Dávila <sup>a,b,c\*</sup>, Linda Luquot <sup>a,b</sup>, Josep M. Soler <sup>a,b</sup> and Jordi Cama <sup>a,b</sup>

4 <sup>a</sup> Institute of Environmental Assessment and Water Research (IDAEA), CSIC.

5 Jordi Girona 18-26, 08034 Barcelona, Catalonia, Spain.

6 <sup>b</sup> Associated Unit: Hydrogeology Group (UPC-CSIC).

7 <sup>c</sup> Department of Civil and Environmental Engineering, Universitat Politècnica de Catalunya (UPC).

8 Jordi Girona 1-3, 08034 Barcelona, Catalonia, Spain.

9 \*Corresponding author: Gabriela Dávila (gabgeo@cid.csic.es)

10 Jordi Girona 18-26, Barcelona 08034. Catalonia, Spain

11 Tel #:+34 934006100

12 Fax #: +34932045904

13 **Abstract**

14 The circulation of CO<sub>2</sub>-rich solutions through fractured marl cores (caprock) under  
15 different flow rates and supercritical CO<sub>2</sub> conditions ( $P_{Total} = 150$  bar,  $pCO_2 = 61$  bar  
16 and  $T = 60$  °C) led to mineral changes caused mainly by calcite dissolution and to a  
17 lesser extent by aluminosilicate dissolution, and by gypsum precipitation adjacent to the  
18 fracture walls. Another significant result was the formation of the altered and highly  
19 porous zone (Dávila et al., 2016a). Dissolution structures ranged from face to uniform  
20 dissolution and wormhole formation depending mainly on the flow rate.

21 2D reactive transport models were used to interpret the results of the percolation  
22 experiments (except at 60 mL h<sup>-1</sup>). They reproduced the variation in the outflow  
23 composition with time and the observed width of the altered zone along the fractures. A  
24 good match was achieved by using initial  $D_{eff}$  values in the rock matrix that ranged from  
25  $1 \times 10^{-13}$  m<sup>2</sup> s<sup>-1</sup> to  $3 \times 10^{-13}$  m<sup>2</sup> s<sup>-1</sup> under slow flow rates. The  $D_{eff}$  value was higher by a  
26 factor of 20 ( $6 \times 10^{-12}$  m<sup>2</sup> s<sup>-1</sup>) under fast flow. Moreover, a slight variation in the calcite  
27 reactive surface areas contributed to the fit of the model to the experimental data.

28 The modeling results reproduced major dissolution of calcite and gypsum precipitation,  
29 and minor dissolution of clinocllore. Calcite dissolution was boosted by increasing the  
30 flow rate and gypsum precipitation increased at intermediate flow rate (1 mL h<sup>-1</sup>). Minor

31 precipitation of dolomite, kaolinite, boehmite and three zeolites (mesolite, stilbite and  
32 smectite) along the altered zone occurred. The magnitude of these reactions was  
33 consistent with the measured increase in porosity over the altered zone.

34 Keywords: CO<sub>2</sub> sequestration, numerical modeling, leakage, marl caprock, calcite  
35 dissolution, gypsum precipitation.

## 36 **1. Introduction**

37 Leakage of injected CO<sub>2</sub> in deep reservoirs may occur through preferential pathways  
38 such as faults and fractures (Rutqvist and Tsang, 2002) and through the rock cement  
39 interface (Dávila et al., 2016b). Dávila et al. (2016a) showed that the permeability of the  
40 Hontomín marl caprock composed of  $\approx 71$  wt.% calcite,  $< 25$  wt.% clay and 10 wt.%  
41 quartz was at least 6 orders of magnitude smaller than fracture permeability ( $k_f$ ) in  
42 fractured cores. Fluids will therefore flow preferentially through fractures, where the  
43 interaction between CO<sub>2</sub>-rich fluids and the rock matrix can bring about changes in  
44 physical and chemical properties caused by dissolution and precipitation (Singurindy  
45 and Berkowitz, 2005; Edlmann et al., 2013; Kampman et al., 2014; Chen et al., 2014;  
46 Dávila et al., 2016a). The interpretation of the processes is not straightforward given  
47 that caprocks are usually composed of a large number of minerals that react differently.

48 Reactive transport modeling has been performed to assess the impact of the  
49 interaction between CO<sub>2</sub>-rich brines and caprocks at the laboratory (Gherardi et al.,  
50 2007; Credo et al., 2009; Hao et al., 2013; Tian et al., 2014) and field scales (Gaus et  
51 al., 2005).

52 Gherardi et al. (2007) modeled fluid-rock interactions in intact and fractured  
53 carbonate-rich shale caprocks using 1D and 2D models, respectively. The dominant role  
54 of calcite outweighed the effects of the other mineralogical changes involving  
55 precipitation/dissolution of Al-silicate minerals. Minor mineral transformations induced  
56 by the advance of the CO<sub>2</sub>-induced acidic front in the caprock included clay dissolution  
57 (illite, chlorite and muscovite) and precipitation reactions (Na-smectite). Other effects  
58 entailed the formation of new minerals such as dawsonite, siderite, and ankerite.

59 Credo et al. (2009) performed and simulated batch experiments with clayey and  
60 clay limestone crushed caprocks at  $p\text{CO}_2 = 150$  bar and  $T = 80$  °C for 90 days. The  
61 reactivity of the two rock samples was similar under these experimental conditions.

62 Dissolution of calcite and dolomite predominated together with minor or negligible  
63 precipitation of kaolinite and montmorillonite due to the destabilization of Ca-  
64 montmorillonite and illite. At a large scale, Tian et al. (2014) performed 1D numerical  
65 simulations of a 30 m long vertical column with 1 m<sup>2</sup> of cross-sectional area to study  
66 the effect of the mineral composition of clay-rich shale and mudstone caprocks at 101  
67 bar and 47 °C. The mineral composition of the caprock controlled the trend of porosity  
68 change. The buffering capacity of the clay-rich shale was higher than that of the  
69 mudstone. The porosity was influenced more by the mineral assemblage of the  
70 mudstone than by the clay-rich shale. This study suggested that the mudstone was more  
71 suitable for use as a caprock.

72 Hao et al. (2013) used a 3D continuum-scale reactive transport model to  
73 simulate core flood experiments for marly dolostone and vuggy limestone reacting with  
74 brines equilibrated with  $p\text{CO}_2 = 5, 10, 20, 30$  bar and  $T = 60$  °C that were performed by  
75 Smith et al. (2013). The authors showed the role of physical heterogeneities on the  
76 carbonate rocks in the development of the dissolution fronts. Stable dissolution fronts  
77 developed in the marly dolostone were fitted using an empirical exponent ( $n = 3$ ) in the  
78 Kozeny–Carman equation for porous media ( $K = K_o \cdot (\phi/\phi_o)^n$ , where  $K$  and  $\phi$  are  
79 permeability and porosity). For more impermeable and heterogeneous cores (vuggy  
80 limestone)  $n = 6-8$ .

81 At field scale, Gaus et al. (2005) evaluated the long term geochemical behavior  
82 of silty clay caprock at the Sleipner injection site by performing 1D reactive transport  
83 modeling combining reaction kinetics and diffusive transport under CO<sub>2</sub> supercritical  
84 conditions ( $P_{Total} = 101.3$  bar;  $p\text{CO}_2 = 100$  bar and  $T = 37$  °C). If the caprock is assumed  
85 to be a homogeneous medium, feldspar alteration would be the dominant long term  
86 reaction despite initial carbonate dissolution. These reactions could cause a slight  
87 decrease in porosity and a subsequent decrease in permeability.

88 In our study, 2D reactive transport modeling was performed to quantify the  
89 dissolution and precipitation processes that occurred in the laboratory percolation  
90 experiments in which CO<sub>2</sub>-rich solutions circulated through fractured marl cores (Dávila  
91 et al., 2016a). The changes in the fractures and in the porosity of the rock matrix  
92 induced by dissolution of calcite, clinocllore, albite and gypsum (in *S-free* solutions)

93 and precipitation of gypsum (in *S-rich* gypsum-equilibrated solutions) and silicate  
 94 minerals led to variations in permeability.

## 95 **2. Summary of the experimental results**

96 Dávila et al. (2016a) showed that the circulation of CO<sub>2</sub>-rich solutions with different  
 97 sulfate contents through fractured cores under supercritical conditions ( $P_{Total} = 150$  bar,  
 98  $pCO_2 = 61$  bar and  $T = 60$  °C) and different flow rates (0.2, 1 and 60 mL h<sup>-1</sup>) resulted in  
 99 a variety of dissolution patterns. In all cases, dissolution of calcite fostered the  
 100 formation of a highly porous reacted zone made up of slowly dissolving grains of  
 101 quartz, illite and pyrite and possible secondary minerals (e.g. gypsum). The dissolution  
 102 and precipitation reactions controlled the variations in the final pore volume associated  
 103 with the reacted cores. In all experiments, an increase in the flow rate led to an increase  
 104 in the calcite dissolution rate and in the final pore volume associated with the reacted  
 105 core. In the *S-rich* solution, the volume of dissolved calcite was always larger than the  
 106 volume of precipitated gypsum. The dissolution of calcite grains and, to a lesser extent,  
 107 the dissolution of clinocllore and albite, created a high porosity zone ( $\phi$  ranged from 48  
 108 to 67 %) along the fracture walls. This porosity zone was composed of non-dissolved  
 109 quartz, pyrite and illite grains, precipitated gypsum (in *S-rich* solutions) and silicate  
 110 phases (e.g., kaolinite or amorphous SiO<sub>2</sub>) and Al-bearing phases (e.g., boehmite).

111 *As regards the dissolution patterns*, in the *S-free* solution experiments face dissolution  
 112 occurred at slow flow rates (pecllet number ( $Pe$ ) of 4 and 21). Wormhole formation was  
 113 observed at the highest flow rate ( $Pe = 1267$ ). However, in *S-rich* solution experiments,  
 114 face dissolution occurred only at the slowest flow rate. At an intermediate flow rate,  
 115 both uniform dissolution and wormhole formation took place. A combination of  
 116 wormhole formation and uniform dissolution occurred at the highest flow rate. Local  
 117 heterogeneities controlled mineral dissolution along the fracture, which could lead to  
 118 unexpected dissolution patterns.

119 *As regards fracture permeability*, under slow flow rates (low  $Pe$ ) and in *S-free* solution  
 120 experiments,  $k_f$  did not significantly change since face dissolution did not cause fracture  
 121 aperture to vary. Moreover, detached grains along the fracture could have led to the  
 122 obstruction of the fluid flow, preventing  $k_f$  from increasing. In *S-rich* solutions, a  
 123 marked decrease in  $k_f$  was attributed to gypsum precipitation. Under fast flow rate (high

124  $Pe$ ),  $k_f$  slightly increased with slight variations in aperture in the *S-free* solution  
 125 experiment. The increase in  $k_f$  in the *S-rich* experiment was attributed to the absence of  
 126 gypsum precipitates. This increase in  $k_f$  suggested the existence of flow through the  
 127 altered rock matrix under these fast flow conditions.

### 128 **3. Reactive transport modeling**

129 The simulations were performed using CrunchFlow code (Steefel et al., 2015). The  
 130 initial mineral composition of the rock was calculated from the initial mineral  
 131 composition obtained from the XRD-Rietveld analysis.

#### 132 **3.1 Description of the CrunchFlow reactive transport code**

133 The reactive transport modeling was performed using the CrunchFlow code (Steefel et  
 134 al., 2015), which solves numerically the mass balance of solutes expressed as

$$135 \quad \frac{\partial(\phi C_j)}{\partial t} = \nabla \cdot (D \nabla C_j) - \nabla \cdot (q C_j) + R_j \quad (j = 1, 2, 3, \dots, n) \quad (1)$$

136 where  $\phi$  is porosity,  $C_j$  is the concentration of component  $j$  ( $\text{mol m}^{-3}$ ),  $q$  is the Darcy  
 137 velocity ( $\text{m}^3 \text{m}^{-2} \text{s}^{-1}$ ),  $R_j$  is the total reaction rate affecting component  $j$  ( $\text{mol m}^{-3} \text{rock s}^{-1}$ )  
 138 and  $D$  is the combined dispersion-diffusion coefficient ( $\text{m}^2 \text{s}^{-1}$ ).

139 The total reaction rate  $R_j$  is given by

$$140 \quad R_j = -\sum_m \nu_{jm} R_m \quad (2)$$

141 where  $R_m$  is the rate of precipitation ( $R_m > 0$ ) or dissolution ( $R_m < 0$ ) of mineral  $m$  in  $\text{mol}$   
 142  $\text{m}^{-3} \text{rock s}^{-1}$ , and  $\nu_{jm}$  is the number of the moles of  $j$  in mineral  $m$ .

143 The reaction rate laws used in the calculations are expressed as

$$144 \quad R_m = A_m \sum_{\text{terms}} k_{m,T} a_{H^+}^{n_{H^+}} \left( \prod_i a_i^{n_i} \right) \left( 1 - \left( \frac{IAP}{K_{eq}} \right)^{m2} \right)^{m1} \quad (3)$$

145 where  $A_m$  is the mineral surface area in  $\text{m}^2_{\text{mineral}} \text{m}^{-3}_{\text{bulk}}$ ,  $k_{m,T}$  is the reaction rate constant  
 146 in  $\text{mol m}^{-2} \text{s}^{-1}$ ,  $a_{H^+}^{n_{H^+}}$  is the term describing the effect of pH on the rate,  $a_i^{n_i}$  is the term  
 147 describing a catalytic/inhibitory effect by another species on the rate,  $IAP$  is the ionic

148 activity product of the solution with respect to the mineral,  $K_{eq}$  is the equilibrium  
 149 constant for the dissolution reaction (ionic activity product at equilibrium) and  $m_2$  and  
 150  $m_1$  are the parameters affecting the dependence of the rate on solution saturation state.  
 151 The rate constant at temperature  $T$  (K) is calculated from

$$152 \quad k_{m,T} = k_{m,25} \exp\left(\frac{E_a}{R} \left(\frac{1}{T_{25}} - \frac{1}{T}\right)\right) \quad (4)$$

153 where  $k_{m,25}$  is the rate constant at 25 °C,  $E_a$  is the apparent activation energy of the  
 154 overall reaction (J mol<sup>-1</sup>) and  $R$  is the gas constant (J mol<sup>-1</sup> K<sup>-1</sup>).

155 Change in mineral surface area ( $A_m$  in m<sup>2</sup><sub>mineral</sub> m<sup>-3</sup><sub>bulk</sub>) owing to dissolution is

$$156 \quad A_m = A^{initial} \left(\frac{\phi_m}{\phi_{(i)m}}\right)^{\frac{2}{3}} \left(\frac{\phi}{\phi_{(i)}}\right)^{\frac{2}{3}} \quad (5)$$

157 Change due to precipitation is

$$158 \quad A_m = A^{initial} \left(\frac{\phi}{\phi_{(i)}}\right)^{\frac{2}{3}} \quad (6)$$

159 where  $\phi_{(i)m}$  is the initial volume fraction of the mineral  $m$  and  $\phi_{(i)}$  is the initial porosity of  
 160 the medium. This formulation ensures that as the volume fraction of a mineral reaches  
 161 zero, so does its surface area. Moreover, in the case of both dissolving and precipitating  
 162 minerals, the term  $(\phi/\phi_{(i)})^{2/3}$  requires the surface area of a mineral in contact with fluid  
 163 to reach zero when the porosity of the medium reaches zero. This formulation is used  
 164 primarily for primary minerals (*i.e.*, minerals with initial volume fractions > 0). In the  
 165 case of secondary minerals which precipitate, the value of the initial bulk surface area  
 166 specified is used provided that precipitation occurs. If this phase subsequently dissolves,  
 167 the above formulation is used with an arbitrary initial volume fraction of 0.01.

### 168 **3.2 Numerical discretization**

169 The 3D cylindrical core samples used for the laboratory experiments (Fig. 1a) were  
 170 converted to a 2D rectangular symmetry. First, half of the circular section of the core  
 171 was transformed into a rectangle. The area of this rectangle was equal to the area of the

172 half circle (area =  $x \cdot l = \frac{1}{2} \cdot \pi \cdot (l/2)^2$ ; where  $l$  is the diameter of the core and  $x$  is the width  
 173 of the rectangle). A 2D longitudinal section of the resulting prism was used as the  
 174 calculation domain (Fig. 1b and c). This domain was composed of a fracture (high  
 175 permeability zone) and rock matrix (low permeability zone; Fig. 1d). The domain was  
 176 divided into 36 and 30 nodes from the inlet to the outlet ( $L$ ) and from the center of the  
 177 fracture to 3.5 mm in the model, respectively (Table 1). Fracture corresponded only to  
 178 the first node in the  $x$  direction. The model considered advection and dispersion only  
 179 along the fracture. Solute transport in the rock matrix was caused only by diffusion.

### 180 3.3 Parameters

#### 181 3.3.1. Rock composition

182 The rock considered in the models was the marl described in Dávila et al. (2016a). It is  
 183 composed of calcite (71.2 wt.%), quartz (9.7 wt.%), illite (7.1 wt.%), albite (6.5 wt.%),  
 184 gypsum (2.0 wt.%), clinocllore (2.8 wt.%), anhydrite (0.5 wt.%), and pyrite (0.2 wt.%).  
 185 The initial porosity of the rock matrix ( $\phi_{(i)}$ ) was estimated by image segmentation  
 186 processing applied to ESEM images, which led to the separation of rock and voids. The  
 187 initial mineral volume fractions were calculated from the estimated porosity (6.7 %;  
 188 Table 2). An analysis of the selection of the secondary minerals was performed based  
 189 on equilibrium batch modeling (Gaus, 2010; Soler et al., 2011; Tian et al., 2014). Initial  
 190 estimates of the reactive surface areas of the primary minerals were calculated by  
 191 assuming spheres with radii estimated from the ESEM images (Table 2). The secondary  
 192 minerals were allowed to start precipitating when the solution reached supersaturation.  
 193 The initial reactive surface areas for all the secondary minerals were assumed to be the  
 194 same and sufficiently high ( $1.0 \times 10^4 \text{ m}^2_{\text{mineral}} \text{ m}^{-3}_{\text{rock}}$ ) to allow fast precipitation (local  
 195 equilibrium). Tutolo et al. (2015) performed simulations and observed that when  
 196 solutions were supersaturated with respect to Al-bearing minerals (boehmite, gibbsite  
 197 and diaspore), only boehmite was taken into account since its precipitation was  
 198 observed under high temperature and pressure conditions.

#### 199 3.3.2. Solution composition

200 The two solutions used in the models were the ones used by Dávila et al., 2016a (Table  
 201 3). In both solutions, the initial concentration of  $\text{CO}_2$  was calculated to be  $6.52 \times 10^{-1}$   
 202  $\text{mol kgw}^{-1}$  according to the Duan and Sun (2003) model with an imposed  $p\text{CO}_2$  of 61

203 bar and bearing in mind that  $P_{Total} = 150$  bar,  $T = 60$  °C and  $I = 0.6$  M. Also, the initial  
 204 concentration of  $O_2$  was estimated to be  $3.06 \times 10^{-4}$  mol  $L^{-1}$  (atmospheric and  $CO_2$ -  
 205 bottle concentrations). The *S-rich* solution was undersaturated with respect to calcite  
 206 ( $SI_{Cal} = -3.20$ ) and near equilibrium with respect to gypsum ( $SI_{Gp} = -0.02$ ) at 60 °C. The  
 207 *S-free* injected solution was undersaturated with respect to both calcite ( $SI_{Cal} = -3.50$ )  
 208 and gypsum ( $SI_{Gp} = -7.54$ ) at 60 °C. The calculated initial pH values were 3.26 and 3.29  
 209 for the *S-rich* and *S-free* solutions, respectively.

210 Since the initial pore water composition of these samples was unknown and disturbed  
 211 during sample preparation, it was assumed to be in equilibrium with calcite and gypsum  
 212 for the *S-rich* solution experiments at room  $T$  and atmospheric  $pCO_2$  (concentration of  
 213  $CO_2 = 4.14 \times 10^{-4}$  mol  $kgw^{-1}$ ), yielding a  $pH \approx 7.7$  (Table 3). A very small concentration  
 214 ( $10^{-6}$  mol  $kgw^{-1}$ ) was assumed for  $Na^+$ ,  $K^+$ ,  $Al^{3+}$ ,  $Cl^-$ ,  $Br^-$ ,  $Fe^{2+}$  and  $SiO_{2(aq)}$ .

### 215 3.3.3. Flow and transport properties

216 Darcy velocity ( $q$ ), initial effective diffusion coefficient ( $D_{eff(i)}$ ), and longitudinal  
 217 dispersivity used in the simulations are shown in Table 2. The flow field used in the  
 218 reactive transport assumed constant Darcy velocity in the fracture and no flow in the  
 219 rock matrix. The effective diffusion coefficient ( $D_{eff}$ ) at 60 °C in the longitudinal and  
 220 transversal directions was calculated as  $D_{eff} = \phi^m D_o$ , where  $m$  is the cementation  
 221 exponent ( $m = 2.5$ ; Revil and Cathles, 1999) and  $D_o$  is the diffusion coefficient in water.

### 222 3.3.4. Thermodynamic and kinetic data

223 One hundred and seven aqueous species were considered in the simulations. The  
 224 equilibrium constants were taken from the EQ3/6 thermodynamic database (Wolery et  
 225 al., 1990) included in CrunchFlow and are listed in Table A1 (Appendix 1). The activity  
 226 coefficients were calculated using the extended Debye-Hückel formulation (b-dot  
 227 model; Helgeson, 1969) with parameters from the same database. Twenty solid phases  
 228 (eight primary minerals (calcite, quartz, illite, albite, gypsum, clinocllore, anhydrite and  
 229 pyrite) and twelve secondary minerals (kaolinite,  $SiO_{2(am)}$ , dolomite, mesolite, stilbite,  
 230 smectite, mordenite, scolecite, analcime, wairakite, laumontite, gismondine and  
 231 boehmite) were considered in the calculations. Equilibrium constants for the mineral  
 232 dissolution reactions (CrunchFlow, EQ3/6) are given in Table A2 (Appendix 1). The  
 233 gypsum equilibrium constant ( $\log K_{Gp}$ ) value at 60 °C used in this study were lower

234 than that initially implemented in the database and were  $\log K_{Gp(60^\circ\text{C})} = -4.7383$  as  
 235 reported by Nordstrom (2013) and Garcia et al. (2014).

236 Kinetic rate laws for the primary and secondary minerals, rate parameters and  
 237 activation energies are listed in Table 4. The mineral dissolution and precipitation rates  
 238 were taken from the literature for each mineral (Palandri and Kharaka, 2004; Xu et al.,  
 239 2012; Bandstra et al., 2008; Bibi et al., 2011; Chou and Wollast, 1985; Hellmann et al.,  
 240 2010; Hamer et al., 2003; Zhang et al., 2015; Domènech et al., 2002; Cama et al.,  
 241 2000). The parallel rate laws for minerals describe the explicit dependence of the rates  
 242 on pH. Rate constants at a temperature different from 25 °C were calculated according  
 243 to Eq. (4).

## 244 **4. Results and discussion**

### 245 **4.1 Dissolution and precipitation reactions**

#### 246 **4.1.1 S-rich injected solution**

247 Adjustment of the values of the mineral reactive surface areas ( $A_m$ ) and the initial  
 248 effective diffusion coefficient ( $D_{eff}$ ) were used to match the variation in aqueous Ca, S,  
 249 Mg, K, Si and Fe concentrations with time (Table 2).

250 Fig. 2 shows the match between the experimental and modeled variations in the output  
 251 concentrations over time in the *S-rich* injected solution experiment at 1 mL h<sup>-1</sup> (*exp. 4*).  
 252 The adjusted surface area of calcite was decreased by one order of magnitude from the  
 253 calculated geometric surface area value to match the output Ca concentration (Table 2),  
 254 which was higher than the input one owing to calcite dissolution (Fig. 2). The increase  
 255 in Ca concentration for the first 8 h was associated with the initially large reactive  
 256 surface area of calcite, resulting in significant calcite dissolution and in a decrease in  
 257 calcite content in the rock matrix close to the fracture. With time, the reaction was  
 258 controlled by diffusion through the rock matrix before slowing down.

259 The experimental and simulated output S concentrations were always smaller than the  
 260 input ones (Fig. 2). The deficit of S was attributed to gypsum precipitation given the  
 261 excessive Ca concentration and the positive values of the gypsum saturation index ( $0 <$   
 262  $SI \leq 0.17$ ) at the outlet of the core during the experiment (Fig. S1; supplementary data).

263 The calculated and measured Mg and K concentrations coincided within error with their  
 264 respective input concentrations.

265 The excess of Fe concentration was due to dissolution of the primary Fe-bearing  
 266 minerals (clinochlore and pyrite). The main Fe source was clinochlore dissolution.  
 267 Although the solutions were highly undersaturated with respect to both minerals at the  
 268 outlet of the core ( $-36.2 < SI_{\text{Cln}} < -29.8$  and  $SI_{\text{Py}} = -200$ ), the amount of pyrite in the  
 269 cores was very small compared to that of clinochlore. The adjusted value of the surface  
 270 area of clinochlore was significantly larger than that calculated using the geometric area  
 271 in order to match the measured Fe concentration (Table 2). Nonetheless, this value is  
 272 not unreasonable for a clay mineral and is similar to  $4.4 \times 10^8 \text{ m}^2_{\text{mineral}} \text{ m}^{-3}_{\text{rock}}$ , which  
 273 was used by Gaus et al. (2005).

274 The considerable output of Si concentration was attributed to the dissolution of albite  
 275 and clinochlore among the silicate minerals (Dávila et al., 2016a). A good match was  
 276 achieved by using values of the surface areas that were significantly larger than the  
 277 values of the geometric surface area. Dissolution of albite and clinochlore was linked to  
 278 the precipitation of clay minerals (smectite and kaolinite), zeolites (mesolite, stilbite,  
 279 scolecite and gismondine) and aluminum oxyhydroxide (boehmite); Table 5). Using the  
 280 same reactive surface area values for all the secondary minerals, calculations showed  
 281 that kaolinite, mesolite and stilbite recorded the highest precipitation. The subsequent  
 282 fall in Si concentration was due to the decrease in reactive surface areas of albite and  
 283 clinochlore. Dissolution of quartz and illite was negligible.

284 Dissolution and precipitation processes occurred during the different experiments and  
 285 influence the outlet pH. Fig. 3a shows the temporal variation of the outlet pH in the  
 286 experiment with *S-rich* injected solution at  $Q = 1 \text{ mL h}^{-1}$  (*exp. 4*). A pH increase up to  
 287 4.4 was calculated in the first 9 h. Thereafter, pH remained fairly constant for 14 h  
 288 before decreasing gently to 4.2 (Fig. 3a). The evolution of the pH with respect to the  
 289 distance normal to fracture and at several positions along the sample is shown in Fig.  
 290 3b. The pH was low at the contact between the fracture wall and the injected solution,  
 291 increasing towards the rock matrix. Differences in pH between the inlet and the outlet of  
 292 the core were minor due to the short residence time of the reacting solution. The pH was  
 293 higher under slow flow rates (4.5, 4.2 and 3.7 at 0.2, 1 and 60  $\text{mL h}^{-1}$ ; Fig. B1;  
 294 Appendix 2).

295 A first prediction of the experimental concentrations in the experiments run at 0.2 and  
 296 60 mL h<sup>-1</sup> was performed using the fitted values of  $D_{eff}$  and  $A_m$  for the primary and  
 297 secondary minerals in *exp. 4* (Fig. 4). This model configuration is labeled model A. We  
 298 observed either overestimation or underestimation of the experimental output  
 299 concentrations for these two extreme flow rate experiments using model A. A better  
 300 match between the experimental and the calculated data was obtained by slightly  
 301 diminishing  $D_{eff}$  in the experiment run under the slow flow rates ( $D_{eff(i)} = 1 - 3 \times 10^{-13} \text{ m}^2$   
 302  $\text{s}^{-1}$  at 0.2 and 1 mL h<sup>-1</sup>) and by increasing  $D_{eff}$  by a factor of 20 at high flow rate ( $D_{eff(i)} =$   
 303  $6 \times 10^{-12} \text{ m}^2 \text{ s}^{-1}$  at 60 mL h<sup>-1</sup>; Table 2). These new model configurations were designated  
 304 model B at 0.2 mL h<sup>-1</sup> and model C at 60 mL h<sup>-1</sup>. Model B led to an approximate fit of  
 305 solution composition at 0.2 mL h<sup>-1</sup>. The fit of model C (60 mL h<sup>-1</sup>) was poorer and not  
 306 much better than that of model A. Furthermore, the  $A_m$  values for the primary and  
 307 secondary species were the same as in model A, regardless of the flow rate (Table 2).  
 308 Dávila et al. (2016a) estimated an increase in the apparent diffusion coefficient by a  
 309 factor of 20 after speeding up the flow rate from 1 to 60 mL h<sup>-1</sup>. This increase could be  
 310 associated with the fact that a fast flow rate would imply less transport control, which is  
 311 reproduced in the model by a large initial  $D_{eff(i)}$  and/or would subsequently result in  
 312 larger alterations and porosities that also require higher diffusion coefficients.

#### 313 4.1.2 *S-free* injected solution

314 Needless to say, in the *S-free* injected solution experiments (Table 3), gypsum did not  
 315 precipitate because of the lack of S in the input solution. Sulfate in solution originated  
 316 from dissolution of primary gypsum and/or anhydrite. An approximate match between  
 317 the measured and the calculated output concentrations was obtained in the experiments  
 318 run at 0.2 and 1 mL h<sup>-1</sup> (Fig. 5) by using the respective  $D_{eff}$  values obtained in the *S-rich*  
 319 solution experiments (Table 2) and the same reactive surface areas of calcite (Table 2).  
 320 However, in the experiment run at 60 mL h<sup>-1</sup>, a wormhole dissolution pattern formed  
 321 (Dávila et al., 2016a). The rectangular geometry of the model domain could not  
 322 reasonably account for the evolution of the cylindrical geometry related to wormholing.  
 323 Discrepancies between the calculated and measured concentrations were therefore to be  
 324 expected (Fig. 5). The temporal evolution of the outlet pH in the experiments with *S-*  
 325 *free* injected solution was similar to that of the outlet pH in the *S-rich* solution  
 326 experiments (Fig. B1; Appendix 2).

## 327 **4.2 Mineral dissolution and precipitation rates**

### 328 **4.2.1 Primary minerals**

329 Fig. 6 shows the variation of the modeled instantaneous mineral reaction rates ( $R_m$ ) with  
 330 respect to distance normal to fracture at the outlet of the core and at different  
 331 experimental times in *exp. 4* (*S-rich* injected solution and  $Q = 1 \text{ mL h}^{-1}$ ). Negative and  
 332 positive rates represent mineral dissolution and precipitation, respectively. Fig. 6 shows  
 333 that the maximum calcite dissolution rate ( $R_{Cal}$ ) decreased with time and moved towards  
 334 the rock matrix. Calcite totally dissolved at the fracture-matrix interface with the  
 335 advance of the reaction front (Fig. 8). The decrease in magnitude of  $R_{Cal}$  is directly  
 336 related to the transport control that changed from advective to diffusive through the rock  
 337 matrix. At the same time, the gypsum precipitation rate ( $R_{Gp}$ ; Fig. 6) at the contact  
 338 between the fracture and rock matrix increased in the first  $\approx 20$  h. This was controlled  
 339 by the Ca supplied from calcite dissolution and  $\text{SO}_4^{2-}$  supplied from the injected  
 340 solution. Thereafter,  $R_{Gp}$  decreased in magnitude because calcite dissolution slowed  
 341 down, diminishing the Ca release. The front of gypsum precipitation followed the  
 342 calcite dissolution front.

343 Clinocllore dissolution rate ( $R_{Cln}$ ) decreased with time and with the reaction moving  
 344 gradually towards the rock matrix. Hence, the Si released from clinocllore dissolution  
 345 fell, undersaturating the solution with respect to albite ( $-4.5 < SI < -10.9$ ; Fig. S1;  
 346 supplementary data) and leading to an increase in the albite dissolution rate ( $R_{Ab}$ ; Table  
 347 4). Otherwise, the calculated quartz dissolution and precipitation rates ( $R_{Qtz}$ ) were  
 348 negligible because of solution acidity. With the concentration of dissolved oxygen in the  
 349 input solution (Table 4) oxidative pyrite dissolution was negligible in the model, since  
 350  $R_{Py}$  was two orders of magnitude slower than that of clinocllore (Fig. 6). Clinocllore  
 351 was therefore the main source of Fe. The anhydrite dissolution rate ( $R_{Anh}$ ) also  
 352 decreased with time and distance normal to fracture. The illite precipitation rate ( $R_{Ill}$ )  
 353 increased initially at the fracture wall and the reaction moved with time towards the  
 354 rock matrix. This reaction was controlled by Al and Si obtained from clinocllore (and  
 355 albite) dissolution.

### 356 4.2.2 Secondary minerals

357 XRD and MicroRaman spectroscopy analyses did not show the presence of any Si  
 358 secondary phase (Dávila et al., 2016a). The measured Al concentrations were always  
 359 close to the ICP-AES detection limit (approximately  $1.85 \times 10^{-6} \text{ mol L}^{-1}$ ), indicating the  
 360 likelihood of Al-bearing phase precipitation given that kaolinite was observed in earlier  
 361 percolation experiments under similar  $p\text{CO}_2$ ,  $T$  and ionic strength conditions (Ketzer et  
 362 al., 2009; Luquot et al., 2012; Yu et al., 2012). In the present study, potential secondary  
 363 minerals included in the model were dolomite,  $\text{SiO}_{2(\text{am})}$ , kaolinite, smectite, mesolite,  
 364 stilbite, mordenite, scolecite, analcime, wairakite, laumontite and gismondine. Initially,  
 365 after 1 h, the calculated dolomite rate ( $R_{Dol}$ ) was positive, indicating dolomite  
 366 precipitation (Figs. 7 and S2; supplementary data). Thereafter, precipitated dolomite  
 367 dissolved adjacent to the fracture wall ( $R_{Dol} < 0$ ) owing to the acidic injected solution,  
 368 whereas precipitation occurred further into the rock matrix because of Mg supplied by  
 369 dissolving clinocllore. In the simulations, precipitation of dolomite was to be  
 370 considered to account for the decrease in Ca concentration over time as well as those of  
 371 S (gypsum precipitation) and Si (mesolite precipitation) concentrations (model D; Fig.  
 372 S4; supplementary data). A poorly crystallized  $\text{SiO}_2$  phase ( $\text{SiO}_{2(\text{am})}$ ) was included in the  
 373 calculations because of Luquot et al. (2012)'s description of its precipitation in similar  
 374 experiments with a S-rich solution and a rich Si-sandstone at  $P_{total} = 100 \text{ bar}$ ,  $p\text{CO}_2 = 60$   
 375 bar and  $T = 95 \text{ }^\circ\text{C}$ . However, our model did not show  $\text{SiO}_{2(\text{am})}$  precipitation.

376 The calculated precipitation rates of kaolinite, mesolite and stilbite were between 5 and  
 377 6 orders of magnitude higher than those of smectite (Figs. 7 and S3; supplementary  
 378 data). The precipitation fronts showed that mesolite ( $R_{Ms}$ ), kaolinite ( $R_{Kln}$ ), stilbite ( $R_{Stl}$ )  
 379 and boehmite ( $R_{Bhm}$ ) rates increased initially at the fracture wall and decreased over  
 380 time. The reactions moved gradually towards the rock matrix. This was controlled by  
 381 the Ca, Al, Si and Fe obtained from mainly calcite and clinocllore dissolution.

### 382 4.3 Variation in mineral volumes

383 Fig. 8 shows the calculated variation in mineral volume fraction (*vol.*%) as a function of  
 384 distance normal to fracture at four different positions along the core in *exp. 4* (S-rich  
 385 solution and  $Q = 1 \text{ mL h}^{-1}$ ). Note that calcite dissolved totally within the first  $\approx 80 \mu\text{m}$   
 386 from the fracture near the inlet ( $L = 0.2 \text{ mm}$ ; Fig. 8) and to a lesser extent further  
 387 downstream along the column. This led to the formation of an altered zone that in the

388 model reached a distance of  $\approx 160 \mu\text{m}$ , which almost coincided with the measured value  
 389 in the ESEM images ( $\approx 176 \mu\text{m}$ ; Dávila et al., 2016a). Hence, the calculated dimensions  
 390 of the altered zone matched fairly well those of the observed dissolution patterns  
 391 (mostly uniform dissolution) in the ESEM and XMT images. Gypsum precipitation was  
 392 significant in the reacted zone, reaching up to 48 *vol.*% at the fracture-rock matrix  
 393 interface (Fig. 8). The amount of precipitated gypsum fell with distance normal to  
 394 fracture and along the fracture following the decrease in calcite dissolution. The change  
 395 between the initial and final volume of anhydrite was negligible. Clinocllore dissolved  
 396 totally over the reacted zone near the inlet. Clinocllore dissolution increased with  
 397 respect to albite and pyrite. Illite precipitation was considerably less.

398 As regards the secondary phases, dolomite precipitated provided that the aqueous Mg  
 399 released from clinocllore dissolution was sufficient to supersaturate the solution (Fig.  
 400 9). The volumes of precipitated kaolinite and boehmite were rather small (up to  $\approx 0.006$   
 401 and  $\approx 0.3 \text{ vol.}\%$ , respectively). The volume of precipitated stilbite ( $\approx 1.8 \text{ vol.}\%$ ) was  
 402 greater than those of mesolite ( $\approx 0.2 \text{ vol.}\%$ ) and smectite (Fig. 9). The small amounts of  
 403 these secondary minerals would render the identification of the secondary phases in the  
 404 ESEM and XMT images very difficult.

405 Fig. 10 illustrates the effect of the flow rate on the variation in calcite volume fraction.  
 406 Calculations show that an increase in the flow rate tended to reduce differences between  
 407 the inlet and the outlet and to increase the penetration length in the altered zone, which  
 408 is consistent with the face dissolution pattern observed for the experiment under slow  
 409 flow rates (Dávila et al., 2016a).

410 Comparison of the volumes of dissolved calcite, gypsum and clinocllore calculated  
 411 from the simulations and from the mass balance equations (Dávila et al., 2016a) shows  
 412 a reasonable match with only a few exceptions. These values are represented by  
 413  $V_{\text{model}}/V_{\text{balance}}$  ratios with values that are significantly different from one (Table 5). In the  
 414 *S-rich* solution experiments run at 0.2 and 1  $\text{mL h}^{-1}$ , the model under or overestimated  
 415 the volume of dissolved calcite because of the influence of  $A_{\text{Cal}}$  in the  $V_{\text{Cal-diss}}$ . Using the  
 416 same  $A_{\text{Cal}}$ ,  $V_{\text{Cal-diss}}$  obtained from the model was greater than that calculated from the  
 417 mass balance, indicating that experimentally less calcite surface was more accessible  
 418 than that assumed in the simulations (Noiriel et al., 2009). By contrast, at the high flow  
 419 rate experiment (*exp.7*) in which wormholing occurred, the model did not reach the

420 amount of precipitated gypsum calculated from the mass balance. This difference was  
 421 attributed to the analytical error between the measured input and output S  
 422 concentrations and to the wormhole formation, which cannot be reproduced by the  
 423 model. In the case of the *S-free* solution experiment at 1 mL h<sup>-1</sup>, the model  
 424 overestimated the volume of dissolved clinocllore calculated from mass balance, which  
 425 was attributed to the mineral heterogeneity of the samples.

#### 426 **4.4 Variation in porosity**

427 Fig. 11 shows the calculated variation in porosity ( $\Delta\phi = \phi_{(f)} - \phi_{(i)}$ ) with respect to  
 428 distance normal to fracture at the outlet of the core at the end of each experiment.  
 429 Porosity increased in the altered zone at the contact between the fracture and the rock  
 430 matrix (e.g.,  $\Delta\phi$  increased up to 70 % in the *S-free* solution experiments). Porosity  
 431 variation decreases with distance normal to fracture, and overall, its variation is similar  
 432 to that estimated from the ESEM images of the thin section ( $\phi = 60$  %; *exp 4*; Fig.  
 433 12a,c). In both types of solution, an increase in the flow rate led to a larger increase in  
 434 porosity (Figs. 11 and 12). Wormhole was more evident in the *S-free* solution  
 435 experiment (Table 5).

436 Overall, the increase in porosity was higher in *S-free* solution experiments than in *S-*  
 437 *rich* solution ones. At low flow rates (0.2 - 1 mL h<sup>-1</sup>), this contrasts with the tendency of  
 438 fracture permeability ( $k_f$ ), which decreased in the *S-rich* experiments and remained  
 439 fairly constant in the *S-free* experiments (Dávila et al., 2016a). This behavior suggests  
 440 that at low flow rates,  $k_f$  was not strictly related to the dissolution and precipitation  
 441 reactions during fracture evolution, but could be influenced by the movement of grains  
 442 in the fracture causing changes in pore structure (Fig. 12). The calculated porosity in the  
 443 *S-free* solution experiments was higher at the high flow rate (60 mL h<sup>-1</sup>; *exp 6*; Fig. 12b)  
 444 than at slow flow rates. However, the calculated porosity was lower in the *S-rich*  
 445 solution experiments than in the *S-free* solution experiments. Moreover,  $k_f$  showed an  
 446 increase, which was larger in the *S-rich* solution experiments. This increase in  $k_f$  was  
 447 expected in a porous medium, in which an increase in porosity yielded a rise in  
 448 permeability.

## 449 **5. From the laboratory to the field scale**

450 The experimental and modeling results of the percolation experiments shown in the  
451 current paper and in the previous one by Dávila et al. (2016a) indicate that both the  
452 formation of dissolution patterns and the variation in fracture permeability are highly  
453 dependent on the flow rate which, being the fracture volume practically the same in all  
454 the experiments, determines the residence time of the fluid circulating through the  
455 fractures. An increase in the residence time (slow flow rate) provokes significant  
456 dissolution of calcite only at the fracture inlet, forming face dissolution patterns, and  
457 allows for gypsum precipitation, yielding either little variation or a reduction in fracture  
458 permeability. Oppositely, shorter residence times (fast flow rate) do not allot for large  
459 changes in solution composition, resulting in the formation of wormholes or uniform  
460 dissolution and an increase in fracture permeability.

461 The residence time in the experiments ranged from 0.1 to 12 s (Table 2), which is  
462 extremely short compared to likely residence times in caprock fractures during CO<sub>2</sub>  
463 injection (e.g., from years, Bachu et al., 1994). Hence, according to our short-term  
464 laboratory-scale results, it can be concluded that the slower flow rates in the repository  
465 system will lead to limited calcite dissolution and effective gypsum precipitation, which  
466 would in turn promote little change or even a decrease in fracture permeability. This  
467 important role of flow velocity has already been pointed out by Brunet et al. (2016) for  
468 Portland cement - CO<sub>2</sub> - brine interactions.

469 At this point, however, we would like to emphasize that the 2D reactive transport  
470 modeling applied to quantify the ongoing processes in the short fractured percolation  
471 experiments under  $p\text{CO}_2$  and temperature similar to those at the field site cannot be  
472 directly used to predict the long-term behavior in caprock fractures at the field scale.  
473 For such modeling, parameters like (1) the dimensions (aperture and length) and  
474 morphology of the field-scale fractures, (2) the reactive mineral surface areas, and (3)  
475 the fluid flow regime should be known. Without this information, a sensitivity analysis  
476 considering the possible variability of these parameters should be performed. Such a  
477 modeling exercise is clearly beyond the objectives of this study.

## 478 6. Summary and conclusions

479 Two dimensional reactive transport models were employed to interpret the results from  
 480 percolation experiments with single fracture marl cores during the injection of CO<sub>2</sub>-rich  
 481 solutions under supercritical conditions ( $P_{Total} = 150$  bar,  $pCO_2 = 61$  bar and  $T = 60$  °C).  
 482 In the model, flow circulated through the fracture, and solute transport in the rock  
 483 matrix was caused only by diffusion. Calculated solution concentration of the outlet  
 484 compares fairly well with the variation in the measured concentrations under slow flow  
 485 rates whereas under fast flow a poor match was obtained. The simulations reproduced  
 486 the dimensions of the dissolution patterns observed in ESEM and XMT images, except  
 487 for the *S-free* experiment run under high flow rate ( $60 \text{ mL h}^{-1}$ ) in which a wormhole  
 488 formed (Dávila et al., 2016a) in a porous altered zone. These results considerably  
 489 improve our understanding of the different dissolution and precipitation processes  
 490 observed during the percolation experiments.

491 A successful match (except for the fast flow rate) between the experimental and  
 492 calculated output concentrations was achieved by using  $D_{eff}$  values between 1 and  $3 \times$   
 493  $10^{-13} \text{ m}^2 \text{ s}^{-1}$  and a single value for calcite irrespective of the type of solution with the  
 494 same reactive surface area ( $1.9 \pm 1.5 \times 10^4 \text{ m}^2_{\text{mineral}} \text{ m}^{-3}_{\text{rock}}$ ). In the fast flow rate  
 495 experiments ( $60 \text{ mL h}^{-1}$ ) to provide more calcite reactivity, the  $D_{eff}$  value showed a  
 496 slight increase ( $6 \times 10^{-12} \text{ m}^2 \text{ s}^{-1}$ ) along with the calcite reactive surface area ( $2.5 \pm 0.1 \times$   
 497  $10^5 \text{ m}^2_{\text{mineral}} \text{ m}^{-3}_{\text{rock}}$ ). The surface area values of the other minerals did not change.

498 Different compositions of the injected solutions produced diverse effects on the mineral  
 499 dissolution and precipitation reactions in the Hontomín caprock. The main reaction that  
 500 occurred was dissolution of calcite in both types of injected solution. For the same  
 501 experimental time and under the same flow rate, the volume of dissolved calcite was  
 502 always larger in the *S-free* solution experiments than in the *S-rich* ones. In *S-rich*  
 503 solution experiments, gypsum precipitated more at  $1 \text{ mL h}^{-1}$ . Dissolution of clinocllore,  
 504 albite, illite and pyrite, and precipitation of dolomite, illite, kaolinite, mesolite, smectite,  
 505 stilbite and boehmite also occurred. Precipitation of secondary Al and Si rich minerals  
 506 took place to a lesser extent as was expected from the mass balance calculations, but  
 507 this was not observed in the ESEM and XMT images.

508 The calcite dissolution rate at the contact between the fracture and the rock matrix,  
 509 where the acid solution reacted with calcite under an advective flow regime, was faster

510 than the rates calculated as the reaction moved towards the rock matrix. This occurred  
511 because the accessibility of the solution to the calcite surface diminished during the  
512 formation of the altered zone where solute transport was controlled by diffusion. This  
513 phenomenon did not occur under the fast-flow rate experiment.

514 In both types of solution, the calculated porosity in the reacted zone was higher at the  
515 fracture wall contact, decreasing with distance normal to fracture. An increase in the  
516 flow rate caused a rise in porosity. The increase in porosity was higher at the inlet of the  
517 core than at the outlet. This difference is diminished after speeding up the flow rate. The  
518 rise in porosity from 6.7 % to  $\approx 70$  % was similar to the volume of dissolved calcite ( $\approx$   
519 60 %).

520 In contrast to the porosity increase, fracture permeability under slow flow rates tended  
521 to decrease in the *S-rich* experiments and remained fairly constant in *S-free*  
522 experiments. In both types of solution, the calculated porosity was greater under the fast  
523 flow rate ( $60 \text{ mL h}^{-1}$ ) than under slow flow rates and  $k_f$  was considerably higher in the *S-*  
524 *free* injected solution. A new model accounting for the wormhole formation is  
525 warranted to fully interpret the results from the experiments run under fast flow.

## 526 **Acknowledgements**

527 This work was financed by projects CGL2010-20984-C02-01 and CGL2014-54831-C3-  
528 1-R of the Spanish Government, project 2014SGR (Grup de Recerca SGR) 1456 of the  
529 Catalan Government and the PANACEA project (European Community's Seventh  
530 Framework Programme FP7/2007-2013 under grant agreement number 282900).  
531 Support was provided for GD by a JAE-Predoc grant under the Program "Junta para la  
532 Ampliación de Estudios", and for LL by a Juan de la Cierva postdoctoral grant  
533 (MINECO, Spain). We would like to thank Natàlia Moreno and Jordi Bellés (IDAEA),  
534 and Eva Pelegrí and Maite Romero (SCT-Barcelona University) for analytical  
535 assistance. We also wish to thank the anonymous reviewers for their constructive  
536 comments that have improved the quality of the paper.

## 537 **Appendix 1**

538 **Table A1** Equilibrium constants ( $\log K_{eq}$ ) for the homogeneous reactions considered in  
539 the reactive transport model. Reactions are written as the dissolution of 1 mol of the

540 species in the table and in terms of  $\text{Ca}^{2+}$ ,  $\text{Mg}^{2+}$ ,  $\text{HCO}_3^-$ ,  $\text{H}^+$ ,  $\text{SO}_4^{2-}$ ,  $\text{Na}^+$ ,  $\text{K}^+$ ,  $\text{Al}^{3+}$ ,  $\text{Cl}^-$ ,  
541  $\text{Br}^-$ ,  $\text{Fe}^{2+}$ ,  $\text{SiO}_{2(\text{aq})}$  and  $\text{O}_{2(\text{aq})}$ .

542 **Table A2** Mineral and gas equilibrium constants ( $\log K_{eq}$ ) considered in the reactive  
543 transport model. Reactions are written as the dissolution of 1 mol of the species  $\text{Ca}^{2+}$ ,  
544  $\text{Mg}^{2+}$ ,  $\text{HCO}_3^-$ ,  $\text{H}^+$ ,  $\text{SO}_4^{2-}$ ,  $\text{Na}^+$ ,  $\text{K}^+$ ,  $\text{Al}^{3+}$ ,  $\text{Cl}^-$ ,  $\text{Br}^-$ ,  $\text{Fe}^{2+}$ ,  $\text{SiO}_{2(\text{aq})}$  and  $\text{O}_{2(\text{aq})}$ .

545 **Appendix 2**

546 **Figure B1** Simulated pH variation with respect to time in the *S-rich* (left) and in the *S-*  
547 *free* (right) injected solutions at the different flow rates (0.2, 1 and 60  $\text{mL h}^{-1}$ ).

548

549 **References**

- 550 Bachu, S., Gunter, W.D., Perkins, E.H., 1994. Aquifer disposal of CO<sub>2</sub>: Hydrodynamic  
551 and mineral trapping. *Energy Convers. Mgmt.* 35, 269-279.
- 552 Bandstra, J.Z., Buss, H.L., Campen, R.K., Liermann, L.J., Moore, J., Hausrath, E.M.,  
553 Navarre-Sitchler, A.K., Jang, J-H., Brantley S.L., 2008. Appendix: Compilation of  
554 Mineral Dissolution Rates. In S. L. Brantley, J. D. Kubicki, & A. F. White (Eds.),  
555 *Kinetics of Water Rock Interactions*, 737–823. Springer.
- 556 Bibi, I., Singh, B., Silvester, E., 2011. Dissolution of illite in saline–acidic solutions at  
557 25°C. *Geochim. Cosmochim. Acta* 75, 3237–3249.
- 558 Brunet, J.P.L., Li, L., Karpyn, Z.K., Huerta, N.J., 2016. Fracture opening or self-  
559 sealing: Critical residence time as a unifying parameter for cement–CO<sub>2</sub>–brine  
560 interactions. *Int. J. Greenh Gas Con.* 47, 25–37.
- 561 Cama, J., Ganor, J., Ayora, C., Lasaga, C.A., 2000. Smectite dissolution kinetics at 80  
562 °C and pH 8.8. *Geochim. Cosmochim. Acta* 64, 2701–2717.
- 563 Chen, L., Kang, Q., Viswanathan, H.S., Tao, W.Q., 2014. Pore-scale study of  
564 dissolution-induced changes in hydrologic properties of rocks with binary  
565 minerals. *Water Resour. Res.* 50, 9343–9365.
- 566 Chou, L., Wollast, R., 1985. Steady-State kinetics and dissolution mechanisms of albite.  
567 *Am. J. Sci.* 285, 963–993.
- 568 Credo, A., Bildstein, O., Jullien, M., Raynal, J., Pétronin, J-C, Lillo, M., Pozo, C.,  
569 Geniaut, G., 2009. Experimental and modeling study of geochemical reactivity  
570 between clayey caprocks and CO<sub>2</sub> in geological storage conditions. *Energy*  
571 *Procedia* 1, 3445–3452.
- 572 Dávila, G., Cama, J., Galíd, S., Luquot, L., Soler, J.M., 2016b. Efficiency of magnesium  
573 hydroxide as engineering seal in the geological sequestration of CO<sub>2</sub>. *Int. J. Greenh*  
574 *Gas Con.* 48, 171–185.

- 575 Dávila, G., Luquot, L., Soler, J.M., Cama, J., 2016a. Interaction between a fractured  
576 marl caprock and CO<sub>2</sub>-rich sulfate solution under supercritical CO<sub>2</sub> conditions. *Int.*  
577 *J. Greenh Gas Con.* 48, 105–119.
- 578 Domènech, C., Ayora, C., De Pablo, J., 2002. Oxidative dissolution of pyritic sludge  
579 from the Aznalcóllar mine (SW Spain). *Chem. Geol.* 190, 339–353.
- 580 Duan, Z., Sun, R., 2003. An improved model calculating CO<sub>2</sub> solubility in pure water  
581 and aqueous NaCl solutions from 273 to 533 K and from 0 to 2000 bar. *Chem.*  
582 *Geol.* 193, 257–271.
- 583 Edlmann, K., Haszeldine, S., McDermott, C., 2013. Experimental investigation into the  
584 sealing capability of naturally fractured shale caprocks to supercritical carbon  
585 dioxide flow. *Environ. Earth Sci.* 70, 3393–3409.
- 586 Garcia-Rios, M., Cama, J., Luquot, L., Soler J.M., 2014. Interaction between CO<sub>2</sub>-rich  
587 sulfate solutions and carbonate reservoir rocks from atmospheric to supercritical  
588 CO<sub>2</sub> conditions: experiments and modeling. *Chem. Geol.* 383, 107–122.
- 589 Gaus, I., 2010. Role and impact of CO<sub>2</sub>-rock interactions during CO<sub>2</sub> storage in  
590 sedimentary rocks. *Int. J. Greenh. Gas Control* 4, 73–89.
- 591 Gaus, I., Azaroual, M., Czernichowski-Lauriol, I., 2005. Reactive transport modelling  
592 of the impact of CO<sub>2</sub> injection on the clayey caprock at Sleipner (North Sea).  
593 *Chem. Geol.* 217, 319–337.
- 594 Gherardi, F., Xu, T.F., Pruess, K., 2007. Numerical modeling of self-limiting and self-  
595 enhancing caprock alteration induced by CO<sub>2</sub> storage in a depleted gas reservoir.  
596 *Chem. Geol.* 244, 103–129.
- 597 Hamer, M., Graham, R.C., Amrhein, C., Bozhilov, K.N., 2003. Dissolution of  
598 Ripidolite (Mg, Fe-Chlorite) in Organic and Inorganic Acid Solutions. *Soil Sci.*  
599 *Soc. Am. J.* 67, 654–661.
- 600 Hao, Y., Smith, M.M., Sholokhova, Y., Carroll, S.A., 2013. CO<sub>2</sub>-induced dissolution of  
601 low permeability carbonates. Part II: Numerical modeling of experiments. *Adv.*  
602 *Water Resour.* 62, 388–408.

- 603 Helgeson, H.C., 1969. Thermodynamics model of hydrothermal systems at elevated  
604 temperatures and pressures. *Am. J. Sci.* 267, 729–804.
- 605 Hellmann, R., Daval, D., Tisserand, D., 2010. The dependence of albite feldspar  
606 dissolution kinetics on fluid saturation state at acid and basic pH: Progress towards  
607 a universal relation. *C. R. Geosci.* 342, 676–684.
- 608 Kampman, N., Bickle, M., Wigley, M., Dubacq, B., 2014. Fluid flow and CO<sub>2</sub>–fluid–  
609 mineral interactions during CO<sub>2</sub>-storage in sedimentary basins. *Chem. Geol.* 369,  
610 22–50.
- 611 Ketzer, J.M., Iglesias, R., Einloft, S., Dullius, J., Ligabue, R., De Lima, V., 2009.  
612 Water–rock–CO<sub>2</sub> interactions in saline aquifers aimed for carbon dioxide storage:  
613 Experimental and numerical modeling studies of the Rio Bonito Formation  
614 (Permian), southern Brazil. *Appl. Geochem.* 24, 760–767.
- 615 Luquot, L., Andreani, M., Gouze, P., Camps, P., 2012. CO<sub>2</sub> percolation experiment  
616 through chlorite/zeolite-rich sandstone (Pretty Hill Formation – Otway Basin–  
617 Australia). *Chem. Geol.* 294-295, 75–88.
- 618 Noiriél, C., Luquot, L., Madé, B., Raimbault, L., Gouze, P., van der Lee, J., 2009.  
619 Changes in reactive surface area during limestone dissolution: An experimental  
620 and modelling study. *Chem. Geol.* 265, 160–170.
- 621 Nordstrom, D.K., 2013. Improving internal consistency of standard state  
622 thermodynamic data for sulfate ion, portlandite, gypsum, barite, celestine, and  
623 associated ions. *Procedia Earth Planet. Sci.* 7, 624–627.
- 624 Palandri, J.L., Kharaka, Y.K., 2004. A compilation of rate parameters of water-mineral  
625 interaction kinetics for application to geochemical modeling. *science for a  
626 changing world.*
- 627 Revil, A., Cathles III, L.M., 1999. Permeability of shaly sands. *Water Resour. Res.* 35,  
628 651–662.
- 629 Rutqvist, J., Tsang, C.F., 2002. A study of caprock hydromechanical changes associated  
630 with CO<sub>2</sub>-injection into a brine formation. *Environ. Geol.* 42, 296-305.

- 631 Singurindy, O., Berkowitz, B., 2005. The role of fractures on coupled dissolution and  
632 precipitation patterns in carbonate rocks. *Adv. Water Resour.* 28, 507–521.
- 633 Smith, M.M., Sholokhova, Y., Hao, Y., Carroll, S.A., 2013. CO<sub>2</sub>-induced dissolution of  
634 low permeability carbonates. Part I: Characterization and experiments. *Adv. Water*  
635 *Resour.* 62, 370–387.
- 636 Soler, J.M., Vuorio, M., Hautojärvi, A., 2011. Reactive transport modeling of the  
637 interaction between water and a cementitious grout in a fractured rock. Application  
638 to ONKALO (Finland). *Appl. Geochem.* 26, 1115–1129.
- 639 Steefel, C.I., Appelo, C.A.J., Arora, B., Jacques, D., Kalbacher, T., Kolditz, O.,  
640 Lagneau, V., Lichtner, P.C., Mayer, K.U., Meeussen, J.C.L., Molins, S., Moulton,  
641 D., Shao, H., Šimůnek, J., Spycher, N., Yabusaki, S.B., Yeh, G.T., 2015. Reactive  
642 transport codes for subsurface environmental simulation. *Computat. Geosci.* 19,  
643 445-478.
- 644 Tian, H., Xu, T., Wang, F., Patil, V.V., Sun, Y., Yue, G., 2014. A numerical study of  
645 mineral alteration and self-sealing efficiency of a caprock for CO<sub>2</sub> geological  
646 storage. *Acta Geotech.* 9, 87–100.
- 647 Tutolo, B.M., Luhmann, A.J., Kong, X.Z., Saar, M.O., Seyfried, W.E., 2015. CO<sub>2</sub>  
648 sequestration in feldspar-rich sandstone: Coupled evolution of fluid chemistry,  
649 mineral reaction rates, and hydrogeochemical properties. *Geochim. Cosmochim.*  
650 *Acta* 160, 132–154.
- 651 Wolery, T.J., Jackson, K.J., Bourcier, W.L., Bruton, C.J., Viani, B.E., Knauss, K.G.,  
652 Delany, J.M., 1990. Current status of the EQ3/6 software package for geochemical  
653 modeling, in: Melchior, C., Bassett, R.L. (Eds.). *Chemical Modeling of Aqueous*  
654 *Systems II*. ACS Symposium 416, 104–116.
- 655 Xu, J., Fan, C., Teng, H.H., 2012. Calcite dissolution kinetics in view of Gibbs free  
656 energy, dislocation density, and *p*CO<sub>2</sub>. *Chem. Geol.* 322–323, 11–18.
- 657 Yu, Z., Liu, L., Yang, S., Li, S., Yang, Y., 2012. An experimental study of CO<sub>2</sub>-  
658 solution–rock interaction at in situ pressure–temperature reservoir conditions.  
659 *Chem. Geol.* 326-327, 88–101.

660 Zhang, S., Yang, L., De Paolo, D.J., Steefel, C.I., 2015. Chemical affinity and pH  
661 effects on chlorite dissolution kinetics under geological CO<sub>2</sub> sequestration related  
662 conditions. *Chem. Geol.* 396, 208–217.

663

664 **Figure captions**

665 **Figure 1** Schemes showing: *a*) simplified experimental setup (more details in Dávila et  
 666 al., 2016a), *b*) fractured core sample and flow direction, and the spatial discretization  
 667 corresponding to the fractured marl cores: *c*) cylindrical coordinates, *d*) rectangular  
 668 coordinates and *e*) mesh distribution along the core sample.

669 **Figure 2** Variation of the output concentrations with time under  $p\text{CO}_2$  of 61 bar and 60  
 670 °C in *S-rich* injected solution at 1 mL h<sup>-1</sup> (*exp. 4*) for Ca, S, Mg, K, Fe and Si. Solid  
 671 symbols and solid line represent the experimental and calculated variations,  
 672 respectively. The dotted line represents the input solution concentration.

673 **Figure 3** Simulated pH variations of the outlet solution with respect to time (left) and  
 674 with distance normal to fracture and at various positions along the fracture (right) *Exp. 4*  
 675 at  $Q = 1 \text{ mL h}^{-1}$  and *S-rich* injected solution.

676 **Figure 4** Variations in the output species concentrations with time under  $p\text{CO}_2$  of 61  
 677 bar and 60 °C during *S-rich* injected solution experiments at  $Q = 0.2 \text{ mL h}^{-1}$  (*exp. 2*;  
 678 left) and at  $Q = 60 \text{ mL h}^{-1}$  (*exp. 7*; right). Solid symbols and lines represent the  
 679 experimental and calculated (model A, B and C) variations, respectively. The dotted  
 680 line represents the input solution concentration.

681 **Figure 5** Variations in the output concentrations with time under  $p\text{CO}_2$  of 61 bar and 60  
 682 °C in *S-free* injected solution experiments at 0.2, 1 and 60 mL h<sup>-1</sup> (*exps. 1, 3 and 6*): Ca,  
 683 S, Fe and Si.

684 **Figure 6** Variations of the simulated dissolution and precipitation rates of the primary  
 685 minerals ( $\text{mol L}^{-1} \text{ s}^{-1}$ ) with respect to distance normal to fracture at different times at the  
 686 outlet of the core sample, for the 1 mL h<sup>-1</sup> experiment (*S-rich*): calcite (Cal), gypsum  
 687 (Gp), clinocllore (Cln), albite (Ab), quartz (Qtz), pyrite (Py), anhydrite (Anh) and illite  
 688 (Ill).

689 **Figure 7** Variations of the simulated precipitation rates of the secondary minerals ( $\text{mol}$   
 690  $\text{L}^{-1} \text{ s}^{-1}$ ) with respect to distance normal to fracture at different times in a 1 mL h<sup>-1</sup>  
 691 experiment (*S-rich*): dolomite (Dol), mesolite (Ms), smectite (Smc), kaolinite (Kln),  
 692 stilbite (Stl) and boehmite (Bhm).

693 **Figure 8** Variations of the simulated volumes of the primary minerals with distance  
694 normal to fracture at different distances from the inlet: calcite (Cal), gypsum (Gp),  
695 clinocllore (Cln), albite (Ab), illite (Ill) and pyrite (Py).

696 **Figure 9** Variations of the simulated volumes of the secondary minerals with distance  
697 normal to fracture at different distances from the inlet: dolomite (Dol), mesolite (Ms),  
698 smectite (Smc), kaolinite (Kln), stilbite (Stl) and boehmite (Bhm).

699 **Figure 10** Variations of the simulated calcite volume fraction (*vol.%*) with respect to  
700 distance normal to fracture in *S-free* (a) and *S-rich* (b) injected solution experiments at  
701 different flow rates ( $Q$ ). The dashed vertical lines indicate the fracture-rock matrix  
702 interface.

703 **Figure 11** Modeled porosity ( $\Delta\phi$ ) variations along distance normal to fracture at  
704 different flow rates (0.2, 1 and 60 mL h<sup>-1</sup>) at the outlet of the core and at the end of the  
705 experiments under different solution compositions: a) *S-rich* injected solution and b) *S-*  
706 *free* injected solution.

707 **Figure 12** ESEM images from the thin section of the reacted samples of the  
708 experiments under different solution compositions and flow rates: a) *S-rich* injected  
709 solution at 1 mL h<sup>-1</sup> (*exp. 4*), b) *S-free* injected solution at 60 mL h<sup>-1</sup>(*exp. 6*) and c) *S-*  
710 *rich* injected solution 1 mL h<sup>-1</sup> (*exp. 4*) together with the corresponding elemental maps.

711

712 **Table heads**

713 **Table 1** Spatial discretization (number of nodes and grid spacing) used in *exp. 4* at 1  
714 mL h<sup>-1</sup>. In the other experiments length may vary from 18.4 to 19.6 mm.

715 **Table 2** Experimental conditions, flow and transport properties, mineralogical  
716 composition, initial effective diffusion coefficients and reactive surface areas used in the  
717 simulations.

718 **Table 3** Chemical composition, pH and saturation indexes (*SI*) of the injected and  
719 porewater solutions used in the simulations.

720 **Table 4** Reaction rate constants ( $k_{m,25}$ ), activation energies ( $E_a$ ) and rate parameters (Eq.  
721 3) for the mineral reactions considered in the models. The parallel rate laws for minerals  
722 describe the pH dependencies under different pH ranges (a: acid, n: neutral and b:  
723 basic).

724 **Table 5** Volumes of dissolved calcite, gypsum, clinocllore and albite and volumes of  
725 precipitated secondary minerals, calculated from the mass balance (Dávila et al., 2016a)  
726 and the simulations.

**Table 1**

perpendicular to fracture			along fracture		
N Nodes in X	spacing [ $\mu\text{m}$ ]	accumulated distance [ $\mu\text{m}$ ]	N Nodes in Y	spacing [mm]	accumulated distance [mm]
1	8.0	8.0	10	0.39	3.9
2	1.0	10.0	9	0.43	7.8
3	12.7	48.1	8	0.49	11.7
7	16.2	161.5	6	0.65	15.6
10	32.4	485.5	3	1.29	19.4
7	435.0	3530.5			

**Table 2**

		conditions					
		150					
$P$ [bar]		61					
$p\text{CO}_2$ [bar]		60					
$T$ [°C]		0.067					
porosity ( $\phi$ )		2.5					
cementation exponent ( $m$ )		$1.0 \times 10^{-3}$					
longitudinal dispersivity [m]		0.0					
transversal dispersivity [m]							
		parameters					
		S-rich			S-free		
injected solution		exp 2	exp 4	exp 7	exp 1	exp 3	exp 6
experiment label		19.2	19.4	18.4	19.6	18.6	18.7
core length ( $L$ ) [mm]		0.2	1	60	0.2	1	60
$Q$ [mL h <sup>-1</sup> ]		12	10	0.1	10	2	0.1
residence time ( $\tau$ ) [s]		3.8	16.3	16.3	3.2	3.5	14.3
fracture aperture ( $h$ ) [ $\mu\text{m}$ ]		$1.6 \times 10^{-3}$	$1.9 \times 10^{-3}$	$1.1 \times 10^{-1}$	$1.9 \times 10^{-3}$	$8.9 \times 10^{-3}$	$1.3 \times 10^{-1}$
$q$ [m <sup>3</sup> rock m <sup>-2</sup> cell s <sup>-1</sup> ]		$1 \times 10^{-13}$	$3 \times 10^{-13}$	$6 \times 10^{-12}$	$1 \times 10^{-13}$	$3 \times 10^{-13}$	$6 \times 10^{-12}$
$D_{eff(i)}$ [m <sup>2</sup> s <sup>-1</sup> ]							
		experiments					
		S-rich			S-free		
minerals		adjusted surface area [m <sup>2</sup> mineral m <sup>-3</sup> rock]			adjusted surface area [m <sup>2</sup> mineral m <sup>-3</sup> rock]		
	vol. %	grain size (radius in $\mu\text{m}$ )			grain size (radius in $\mu\text{m}$ )		
		[m <sup>2</sup> mineral m <sup>-3</sup> rock]			[m <sup>2</sup> mineral m <sup>-3</sup> rock]		
calcite	66.2	$1.9 \times 10^5$	$1.9 \times 10^4$	$8.5 \pm 0.1 \times 10^4$	$1.9 \pm 1.5 \times 10^4$	$1.9 \pm 1.5 \times 10^4$	$2.5 \pm 0.1 \times 10^5$
quartz	9.2	$1.0 \times 10^4$	$1.0 \times 10^4$	$1.0 \times 10^6$	$1.0 \times 10^6$	$1.0 \times 10^6$	
illite	6.4	$2.0 \times 10^4$	$2.0 \times 10^4$	$2.0 \times 10^6$	$2.0 \times 10^6$	$2.0 \times 10^6$	
albite	6.3	$6.0 \times 10^3$	$6.0 \times 10^3$	$3.5 \times 10^8$	$3.5 \times 10^8$	$3.5 \times 10^8$	
gypsum	2.2	$9.5 \times 10^2$	$9.5 \times 10^2$	$1.0 \pm 0.5 \times 10^1$	$1.0 \pm 0.5 \times 10^1$	$1.0 \pm 0.5 \times 10^1$	
clinocllore	2.6	$3.0 \times 10^3$	$3.0 \times 10^3$	$3.9 \pm 3.6 \times 10^9$	$3.9 \pm 3.6 \times 10^9$	$3.9 \pm 3.6 \times 10^9$	
anhydrite	0.3	$1.5 \times 10^2$	$1.5 \times 10^2$	$1.5 \times 10^2$	$1.5 \times 10^2$	$1.5 \times 10^2$	
pyrite	0.1	$8.1 \times 10^1$	$8.1 \times 10^1$	$1.0 \times 10^6$	$1.0 \times 10^6$	$1.0 \times 10^6$	
kaolinite	-	-	-	$1.0 \times 10^4$	$1.0 \times 10^4$	$1.0 \times 10^4$	
SiO <sub>2(am)</sub>	-	-	-	$1.0 \times 10^4$	$1.0 \times 10^4$	$1.0 \times 10^4$	
dolomite	-	-	-	$1.0 \times 10^4$	$1.0 \times 10^4$	$1.0 \times 10^4$	
zeolites	-	-	-	$1.0 \times 10^4$	$1.0 \times 10^4$	$1.0 \times 10^4$	
boehmite	-	-	-	$1.0 \times 10^4$	$1.0 \times 10^4$	$1.0 \times 10^4$	

\*  $D_{eff(i)}/D_{eff(o)} = (\phi_i/\phi_o)^m$ ;  $D_{eff(i)}$  and  $D_{eff(o)}$  represent the initial and final effective diffusion coefficients, respectively.

**Table 3**

component	injected solutions			initial rock porewater	
	constraints	<i>S-rich</i> concentration [mol kgw <sup>-1</sup> ] or pH	<i>S-free</i> concentration [mol kgw <sup>-1</sup> ] or pH	constraint	concentration [mol kgw <sup>-1</sup> ] or pH
Ca <sup>2+</sup>	known	4.94 × 10 <sup>-2</sup>	2.14 × 10 <sup>-2</sup>	calcite	1.07 × 10 <sup>-2</sup>
Mg <sup>2+</sup>	known	3.22 × 10 <sup>-2</sup>	1.67 × 10 <sup>-2</sup>	fixed	1.00 × 10 <sup>-6</sup>
HCO <sub>3</sub> <sup>-</sup>	known	6.52 × 10 <sup>-1</sup>	6.52 × 10 <sup>-1</sup>	known	equilibrium with CO <sub>2</sub>
pH	charge balance	3.29	3.26	charge balance	7.71
SO <sub>4</sub> <sup>2-</sup>	known	2.62 × 10 <sup>-2</sup>	1.00 × 10 <sup>-9</sup>	gypsum	1.05 × 10 <sup>-2</sup>
Na <sup>+</sup>	known	3.80 × 10 <sup>-1</sup>	1.98 × 10 <sup>-1</sup>	fixed	1.00 × 10 <sup>-6</sup>
K <sup>+</sup>	known	1.10 × 10 <sup>-2</sup>	5.57 × 10 <sup>-3</sup>	fixed	1.00 × 10 <sup>-6</sup>
Al <sup>3+</sup>	known	1.85 × 10 <sup>-6</sup>	1.85 × 10 <sup>-6</sup>	fixed	1.00 × 10 <sup>-6</sup>
Cl <sup>-</sup>	known	5.02 × 10 <sup>-1</sup>	2.80 × 10 <sup>-1</sup>	fixed	1.00 × 10 <sup>-6</sup>
Br <sup>-</sup>	known	1.00 × 10 <sup>-9</sup>	1.00 × 10 <sup>-9</sup>	fixed	1.00 × 10 <sup>-6</sup>
Fe <sup>2+</sup>	known	6.94 × 10 <sup>-9</sup>	6.94 × 10 <sup>-9</sup>	fixed	1.00 × 10 <sup>-6</sup>
SiO <sub>2(aq)</sub>	known	4.34 × 10 <sup>-7</sup>	4.34 × 10 <sup>-7</sup>	fixed	1.00 × 10 <sup>-6</sup>
O <sub>2(aq)</sub>	known	3.06 × 10 <sup>-4</sup>	3.06 × 10 <sup>-4</sup>	fixed	2.84 × 10 <sup>-4</sup>
minerals	abbreviation	<i>SI</i>			
calcite	Cal	-3.20	-3.50		0.00
quartz	Qtz	-2.90	-2.89		-2.00
Illite	Ilt	-19.42	-19.34		-5.92
Albite	Ab	-15.11	-15.26		-10.06
gypsum	Gp	-0.02	-7.54		0.00
clinochlore	Cln	-62.64	-62.68		-37.18
anhydrite	Anh	0.01	-7.52		-0.44
pyrite	Py	-203.52	-217.87		-242.24
kaolinite	Kln	-10.79	-10.55		-0.65
SiO <sub>2(am)</sub>		-3.96	-3.96		-3.28
dolomite	Dol	-6.58	-7.03		-4.46
mesolite	Ms	-18.66	-18.81		-3.93
stilbite	Stl	-31.06	-31.13		-8.62
smectite	Smc	-25.50	-25.54		-12.81
mordenite		-21.92	-21.98		-12.25
scolecite	Scl	-20.58	-20.64		-2.65
analcime	Anc	-12.24	-12.38		-8.10
waikerite		-28.45	-28.51		-10.84
laumontite		-25.04	-25.10		-6.44
gismondine	Gsm	-46.40	-46.53		-3.29
boehmite	Bhm	-2.57	-2.45		1.52

**Table 4**

<i>mineral and chemical composition</i>	$k_{m,25}$ [mol m <sup>-2</sup> s <sup>-1</sup> ]	$n_{H^+}$	$n_{O_2}$	$Ea$ [kcal mol <sup>-1</sup> ]	$m_1$	$m_2$	<i>reference</i>
<i>primary phases</i>							
Calcite (CaCO <sub>3</sub> )	5.01 × 10 <sup>-1 a</sup> 6.46 × 10 <sup>5 n</sup>	1.000 <sup>a</sup>	-	3.44 <sup>a</sup> 5.62 <sup>n</sup>	3.0	1.0	Palandri and Kharaka, 2004; Xu et al., 2012
Quartz (SiO <sub>2</sub> )	1.02 × 10 <sup>-14 n</sup>	-	-	20.95 <sup>n</sup>	1.0	1.0	Palandri and Kharaka, 2004; Bandstra et al., 2008
Illite (K <sub>0.6</sub> Mg <sub>0.25</sub> Al <sub>2.3</sub> Si <sub>3.5</sub> O <sub>10</sub> (OH) <sub>2</sub> )	2.20 × 10 <sup>-4 a</sup> 2.50 × 10 <sup>-13 n</sup> 2.70 × 10 <sup>-1 b</sup>	0.600 <sup>a</sup>	-	11.00 <sup>a</sup> 3.35 <sup>n</sup> 15.30 <sup>b</sup>	1.0	1.0	Bibi et al., 2011
Albite (NaAlSi <sub>3</sub> O <sub>8</sub> )	7.41 × 10 <sup>-9 a</sup> 9.12 × 10 <sup>-13 n</sup> 1.05 × 10 <sup>-17 b</sup>	0.457 <sup>a</sup> -0.572 <sup>b</sup>	-	15.54 <sup>a</sup> 16.69 <sup>b</sup> 16.98 <sup>n</sup>	15.0	0.3	Palandri and Kharaka, 2004; Chou and Wollast, 1985; Hellmann et al., 2010.
Gypsum (CaSO <sub>4</sub> ·2H <sub>2</sub> O)	1.62 × 10 <sup>-3 n</sup>	-	-	15.00 <sup>n</sup>	1.0	1.0	Palandri and Kharaka, 2004
Clinocllore (Mg <sub>2.9</sub> Fe <sub>2.1</sub> Si <sub>3</sub> Al <sub>2</sub> O <sub>10</sub> (OH) <sub>8</sub> )	3.21 × 10 <sup>-10 a</sup>	0.450 <sup>a</sup>	-	16.00 <sup>a</sup>	1.5.0	0.06	Hamer et al., 2003; Zhang et al., 2015
Anhydrite (CaSO <sub>4</sub> )	1.55 × 10 <sup>3 n</sup>	-	-	3.42 <sup>n</sup>	1.0	1.0	Palandri and Kharaka, 2004
Pyrite (FeS <sub>2</sub> )	3.02 × 10 <sup>-8 a</sup> 2.82 × 10 <sup>-5 n</sup>	0.100 <sup>a</sup>	0.500	13.61 <sup>a</sup> 13.61 <sup>n</sup>	1.0	1.0	Domènech et al., 2002
<i>secondary phases</i>							
Kaolinite (Al <sub>2</sub> Si <sub>2</sub> O <sub>5</sub> (OH) <sub>4</sub> )	4.90 × 10 <sup>-12 a</sup> 6.61 × 10 <sup>-14 b</sup> 8.91 × 10 <sup>-18 n</sup>	0.777 <sup>a</sup> -0.472 <sup>b</sup>	-	15.76 <sup>a</sup> 5.31 <sup>b</sup> 4.28 <sup>n</sup>	1.0	1.0	Palandri and Kharaka, 2004
SiO <sub>2</sub> (am)	1.00 × 10 <sup>-9</sup>	-	-	0.00	1.0	1.0	*
Dolomite (CaMg)(CO <sub>3</sub> ) <sub>2</sub> )	6.46 × 10 <sup>-4 a</sup> 2.95 × 10 <sup>-8 n</sup>	0.500 <sup>a</sup>	-	8.63 <sup>a</sup> 12.48 <sup>n</sup>	1.0	1.0	Palandri and Kharaka, 2004
Mesolite (Ca <sub>0.657</sub> Na <sub>0.676</sub> (Al <sub>0.663</sub> Si <sub>1.003</sub> O <sub>1.562</sub> ) <sub>3</sub> ·7.96H <sub>2</sub> O)	1.00 × 10 <sup>-9</sup>	-	-	0.00	1.0	1.0	*
Stilbite (Na <sub>0.136</sub> K <sub>0.006</sub> Ca <sub>1.019</sub> Al <sub>2.18</sub> Si <sub>6.82</sub> O <sub>16.61</sub> ·8.72H <sub>2</sub> O)	1.00 × 10 <sup>-9</sup>	-	-	0.00	1.0	1.0	*
Smectite (Ca <sub>0.025</sub> Na <sub>0.10</sub> Fe <sub>0.7</sub> K <sub>0.2</sub> Mg <sub>1.15</sub> Al <sub>1.25</sub> Si <sub>3.5</sub> O <sub>7</sub> ·H <sub>2</sub> O)	1.00 × 10 <sup>-12</sup>	-	-	0.00	1.0	1.0	Cama et al., 2000
Mordenite (Ca <sub>0.2895</sub> Na <sub>0.361</sub> Al <sub>0.94</sub> Si <sub>5.06</sub> O <sub>12</sub> ·3.468H <sub>2</sub> O)	1.00 × 10 <sup>-9</sup>	-	-	0.00	1.0	1.0	*
Scolecite (CaAl <sub>2</sub> Si <sub>3</sub> O <sub>10</sub> ·3H <sub>2</sub> O)	1.00 × 10 <sup>-9</sup>	-	-	0.00	1.0	1.0	*
Analcime (Al <sub>0.96</sub> Na <sub>0.96</sub> (Si <sub>2.04</sub> O <sub>3.92</sub> )·H <sub>2</sub> O)	1.00 × 10 <sup>-9</sup>	-	-	0.00	1.0	1.0	*
Wairakite (CaAl <sub>2</sub> Si <sub>4</sub> O <sub>12</sub> ·2H <sub>2</sub> O)	1.00 × 10 <sup>-9</sup>	-	-	0.00	1.0	1.0	*
Laumontite (Ca(AlSi <sub>2</sub> O <sub>6</sub> ) <sub>2</sub> ·4H <sub>2</sub> O)	1.00 × 10 <sup>-9</sup>	-	-	0.00	1.0	1.0	*
Gismondine (Ca <sub>2</sub> Al <sub>4</sub> Si <sub>4</sub> O <sub>6</sub> ·9H <sub>2</sub> O)	1.00 × 10 <sup>-9</sup>	-	-	0.00	1.0	1.0	*
Boehmite (AlO(OH))	2.24 × 10 <sup>-8</sup>	-	-	11.36	1.0	1.0	Palandri and Kharaka, 2004

\* Large value of the term  $A \cdot k_{m,T}$  to allow local equilibrium conditions.

a,b and c mean acid, neutral and basic, respectively.

**Table 5**

minerals	primary phases					secondary phases					$V_{Total-diss}$ [mm <sup>3</sup> ]	$V_{Total-ppt}$ [mm <sup>3</sup> ]
	Cal	Ill	Gp	Cln	Ab	Kln	Dol	Ms	Slb	Bhm		
<b>S-rich solution</b>	<b>exp 2; Q = 0.2 mL h<sup>-1</sup></b>											
$\Delta V_{model}$ [mm <sup>3</sup> ]	-2.90	-0.03	0.41	-1.49	-0.01	0.01	0.78	0.19	1.35	0.13	-4.43	2.86
$\Delta V_{balance}$ [mm <sup>3</sup> ]	-2.80	nc	0.39	-3.29	-(0-1.50)	2.13-4.34	nc	nc	nc	nc	-(6.09-7.59)	2.51-4.72
$\Delta V_{model}/\Delta V_{balance}$	1.04	nc	1.05	0.45								
	<b>exp 4; Q = 1 mL h<sup>-1</sup></b>											
$\Delta V_{model}$ [mm <sup>3</sup> ]	-18.84	-0.16	7.05	-3.70	-0.18	0.002	2.01	0.38	2.37	0.31	-22.88	12.13
$\Delta V_{balance}$ [mm <sup>3</sup> ]	-20.34	nc	7.17	-4.51	-(0-2.06)	2.69-5.73	nc	nc	nc	nc	-(24.85-26.91)	9.87-12.90
$\Delta V_{model}/\Delta V_{balance}$	0.93	nc	0.98	0.82								
	<b>exp 7; Q = 60 mL h<sup>-1</sup></b>											
$\Delta V_{model}$ [mm <sup>3</sup> ]	-7.83	-0.17	4.73	-1.21	-0.15	0.001	0.46	-	0.04	0.11	-9.36	6.13
$\Delta V_{balance}$ [mm <sup>3</sup> ]	-9.09	nc	13.98	-1.17	-(0-0.53)	0.59-1.38	nc	nc	nc	nc	-(10.25-10.79)	14.57-15.36
$\Delta V_{model}/\Delta V_{balance}$	0.86	nc	0.34	1.03								
<b>S-free solution</b>	<b>exp 1; Q = 0.2 mL h<sup>-1</sup></b>											
$\Delta V_{model}$ [mm <sup>3</sup> ]	-3.07	-0.03	-0.15	-1.64	-0.01	0.002	0.83	0.12	1.21	0.15	-4.90	2.31
$\Delta V_{balance}$ [mm <sup>3</sup> ]	-3.07	nc	-0.14	-2.29	-(0-1.05)	1.49-3.03	nc	nc	nc	nc	-(5.36-6.41)	1.63-3.17
$\Delta V_{model}/\Delta V_{balance}$	1.00	nc	1.07	0.72								
	<b>exp 3; Q = 1 mL h<sup>-1</sup></b>											
$\Delta V_{model}$ [mm <sup>3</sup> ]	-7.30	-0.03	-0.83	-1.93	-0.02	0.002	0.87	0.13	1.33	0.17	-10.11	2.51
$\Delta V_{balance}$ [mm <sup>3</sup> ]	-7.30	nc	-0.62	-1.53	-(0-0.70)	0.96-1.99	nc	nc	nc	nc	-(8.83-9.53)	1.58-2.61
$\Delta V_{model}/\Delta V_{balance}$	1.00	nc	1.34	1.26								
	<b>exp 6; Q = 60 mL h<sup>-1</sup></b>											
$\Delta V_{model}$ [mm <sup>3</sup> ]	-44.31	-0.15	-2.52	-1.89	-0.15	0.001	0.55	0.03	0.90	0.16	-49.02	1.63
$\Delta V_{balance}$ [mm <sup>3</sup> ]	-45.82	nc	nc	-1.98	-(0-0.90)	(0.98-2.31)	nc	nc	nc	nc	-(47.80-48.70)	19.00-20.33
$\Delta V_{model}/\Delta V_{balance}$	0.97	nc	nc	0.95								

$V_{Total-diss}$  is the total volume of dissolved mineral and  $V_{Total-ppt}$  is the total volume of precipitated mineral.

$\Delta V = V_{final} - V_{initial}$ , where  $\Delta V > 0$  and  $\Delta V < 0$  indicate mineral precipitation and mineral dissolution, respectively.

Values in parentheses indicate the  $\Delta V$  range considering the two hypothetical calculations.

nc indicates that the volume could not be calculated from the mass balance (Ill, Dol, Ms and Stl).

Figure 1

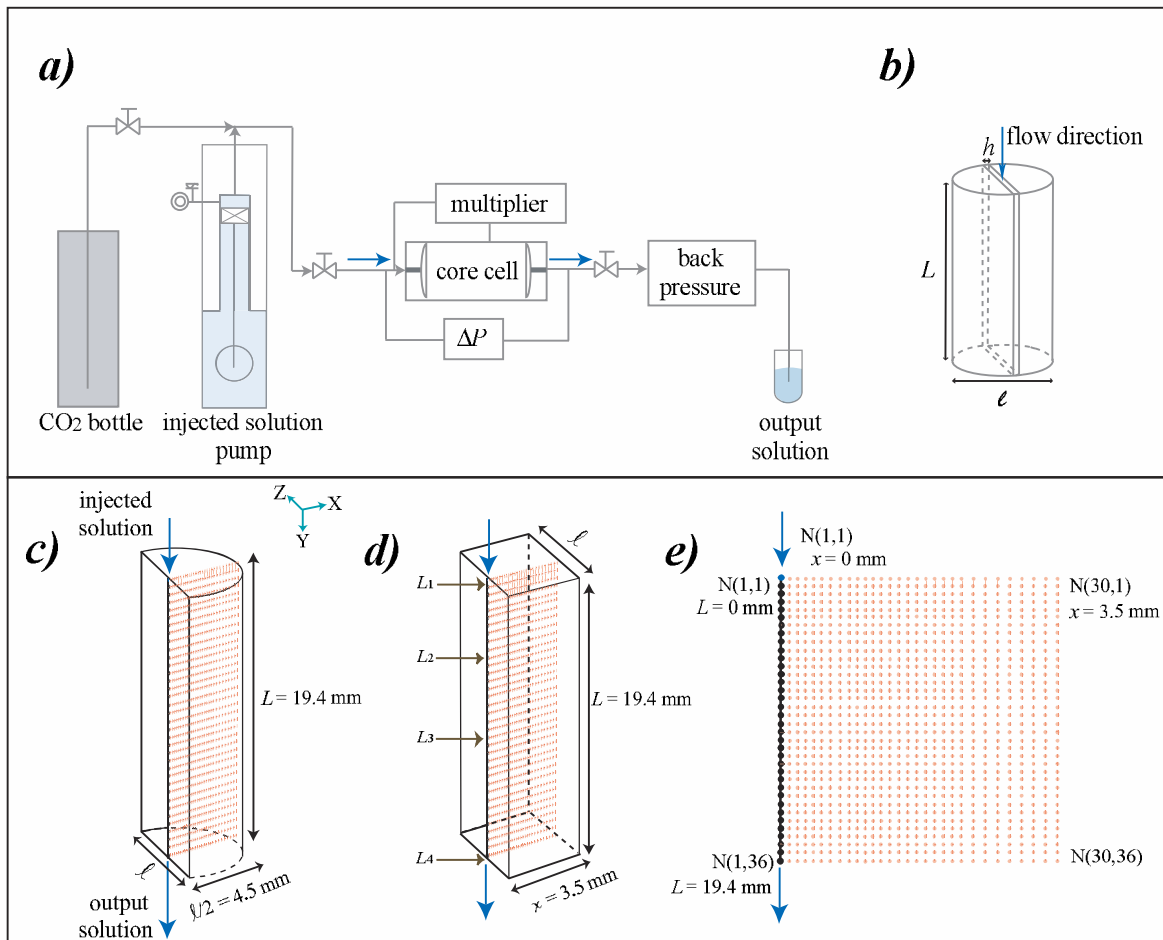


Figure 2

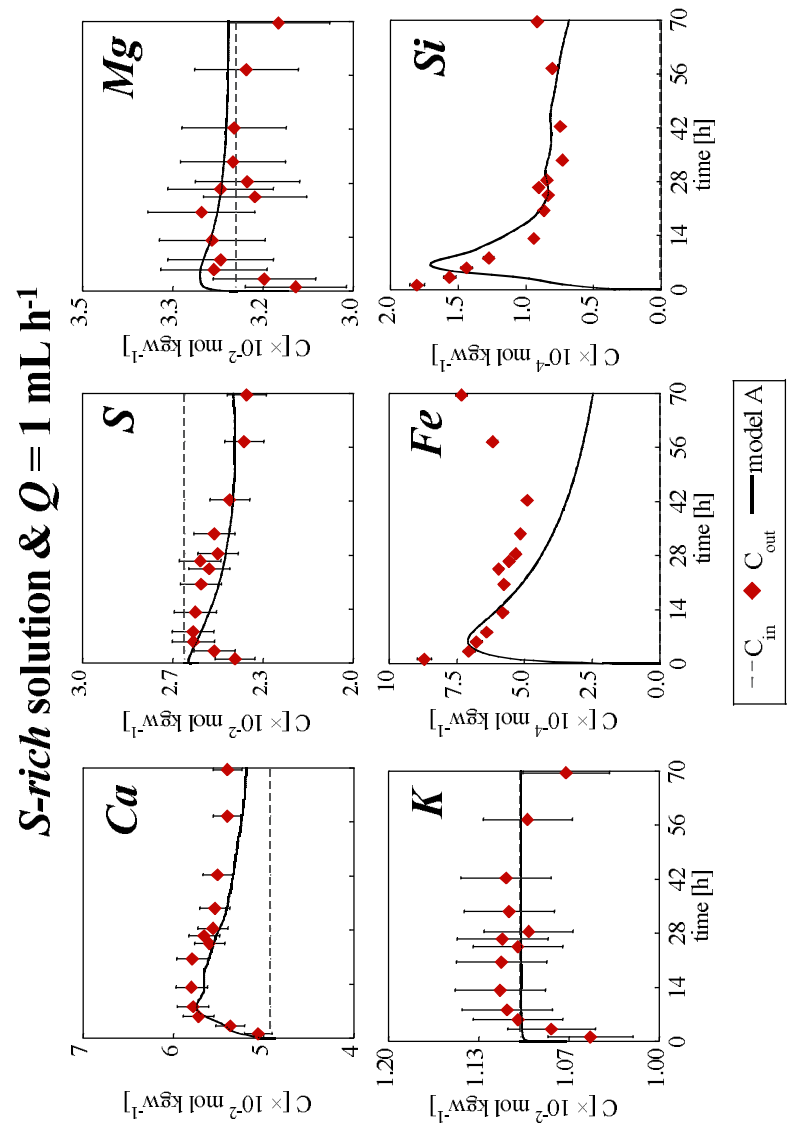


Figure 3

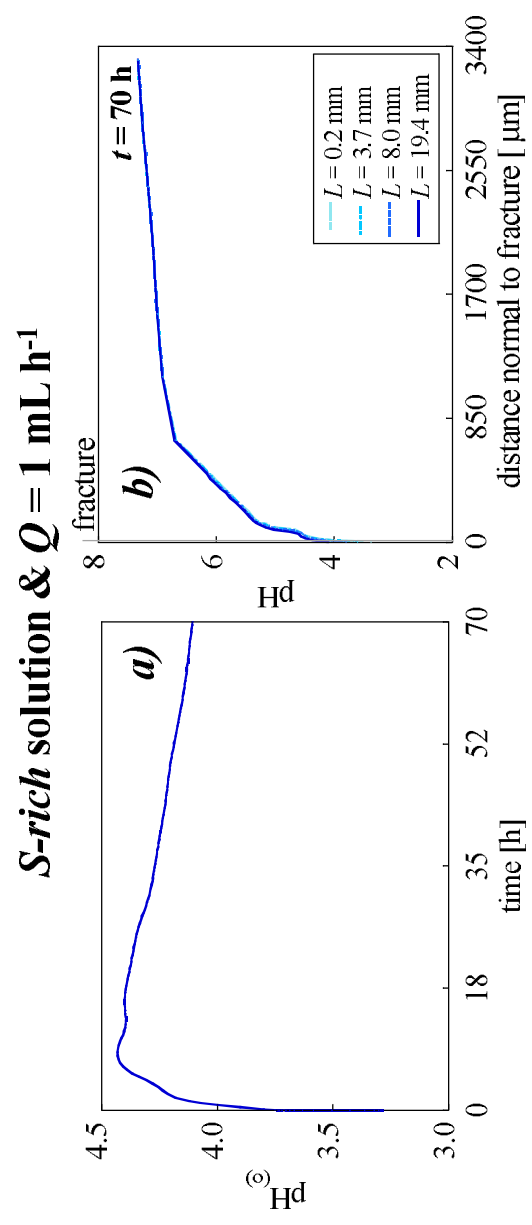


Figure 4

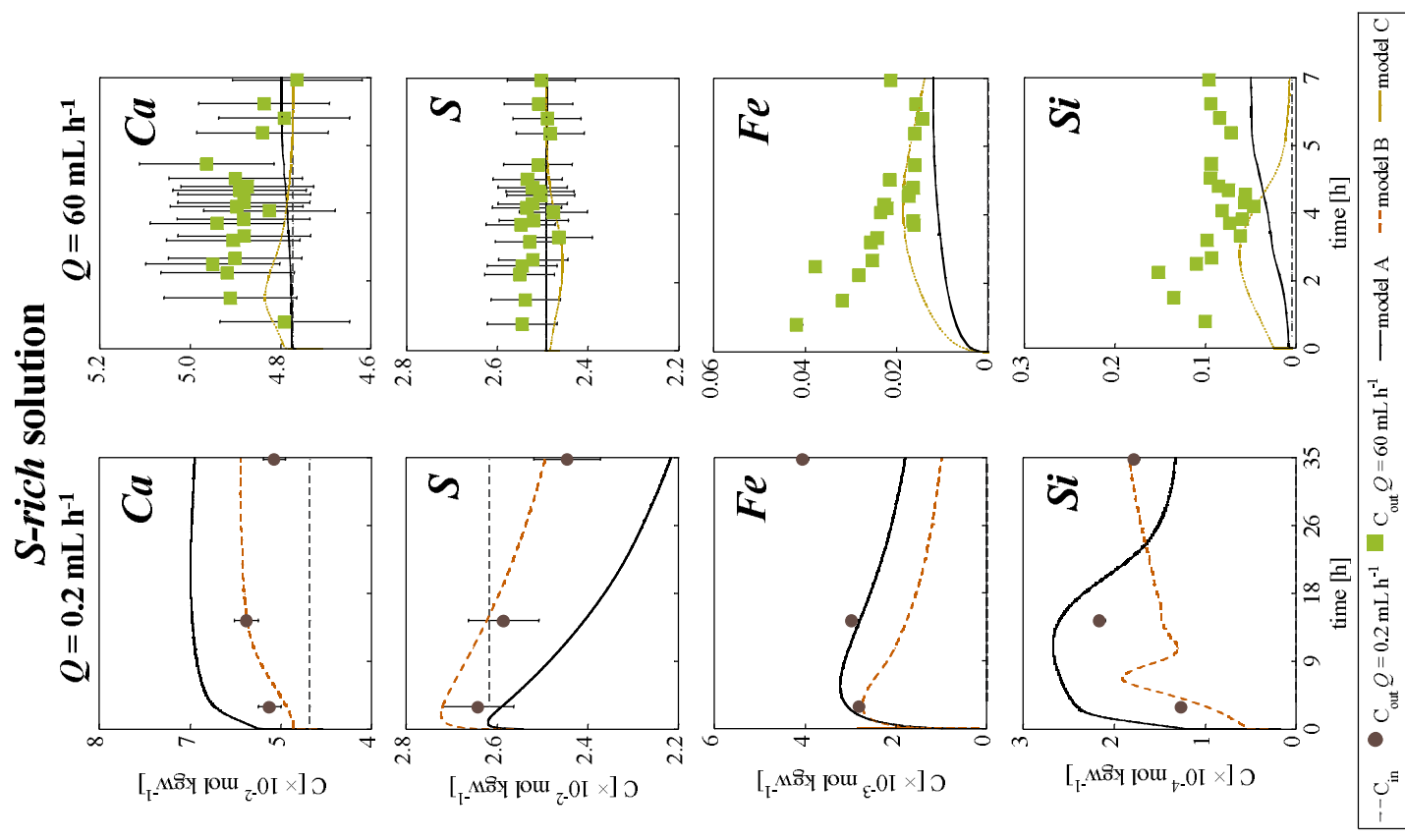


Figure 5

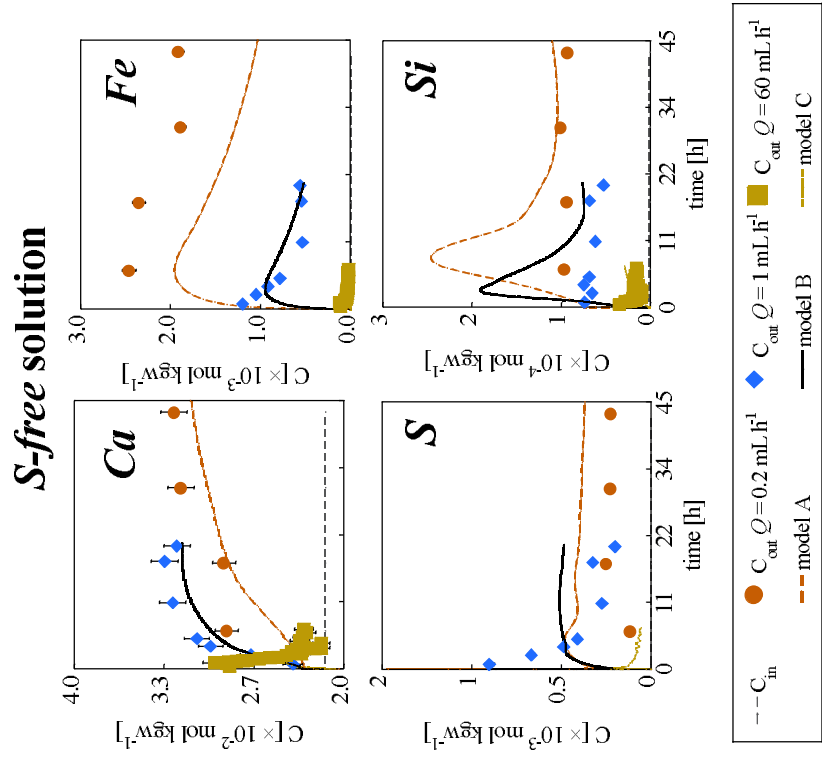


Figure 6

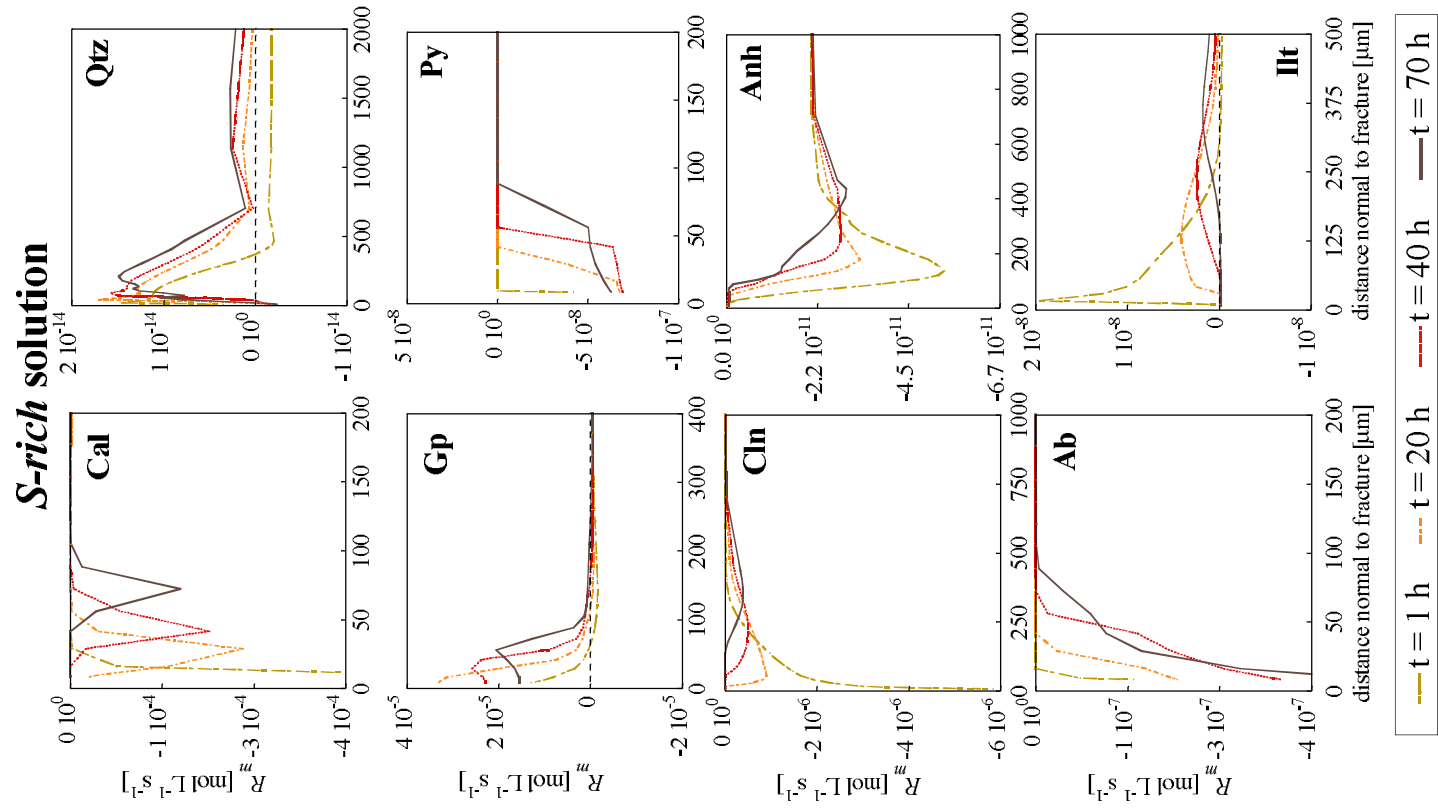


Figure 7

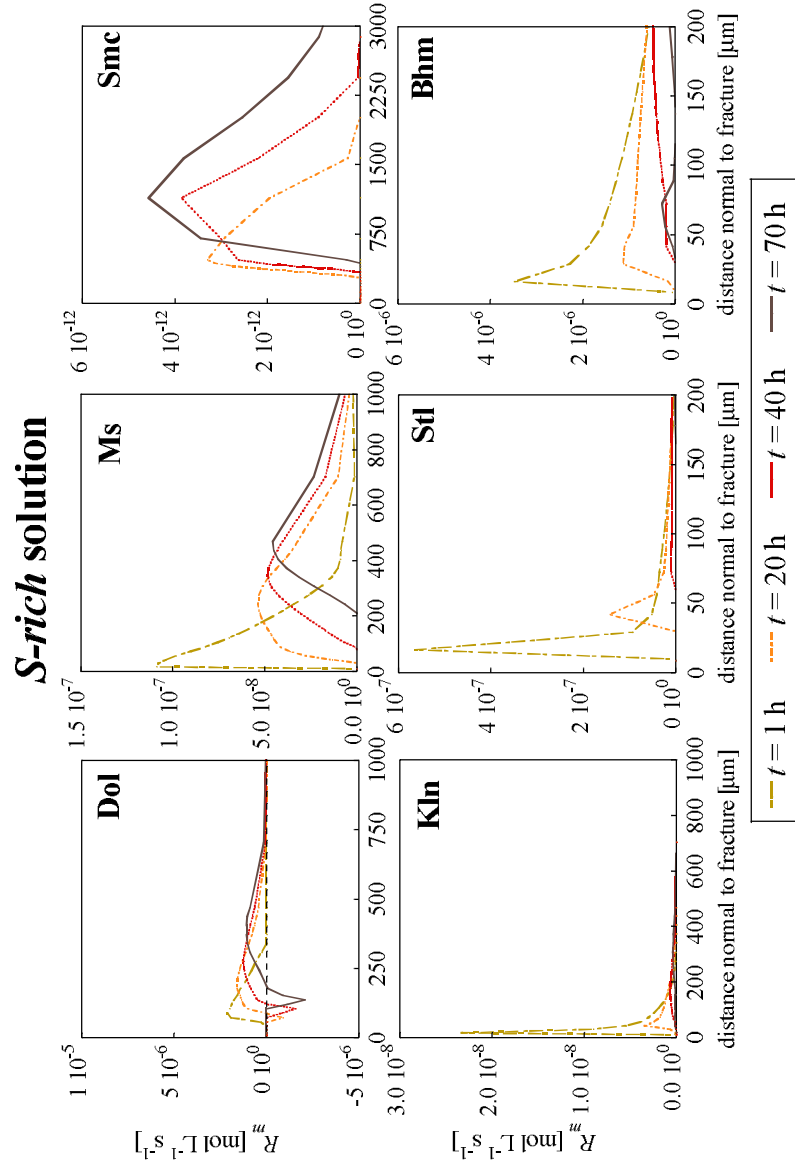


Figure 8

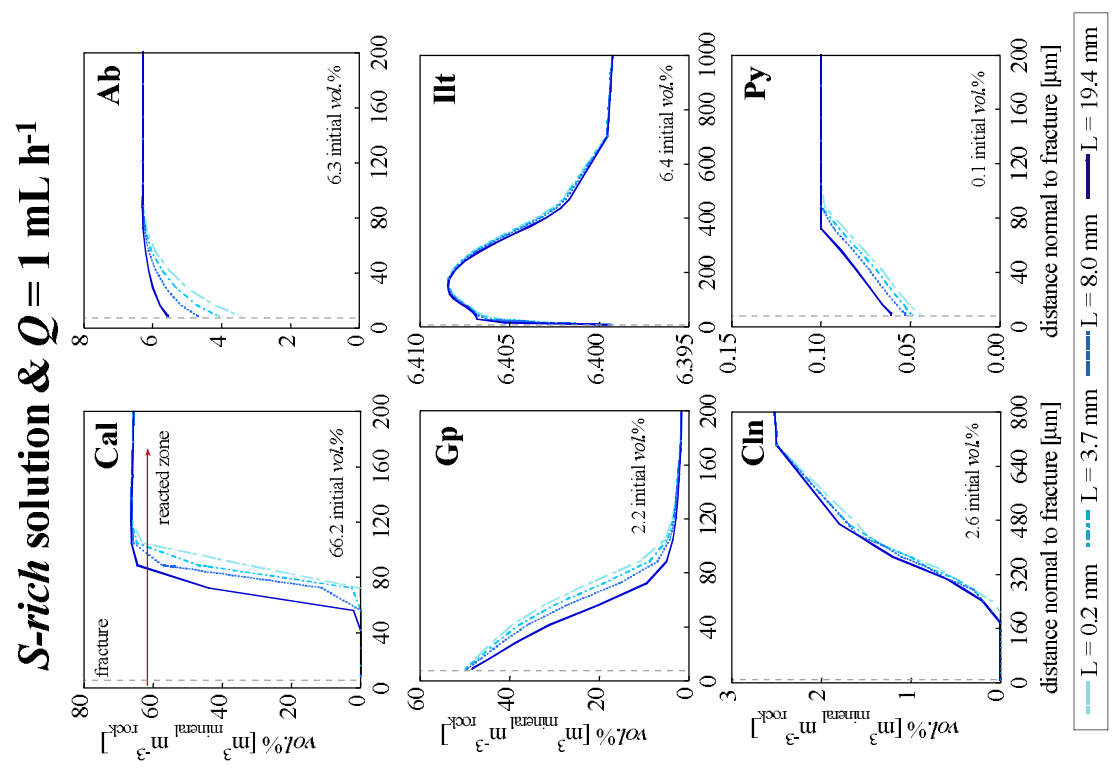


Figure 9

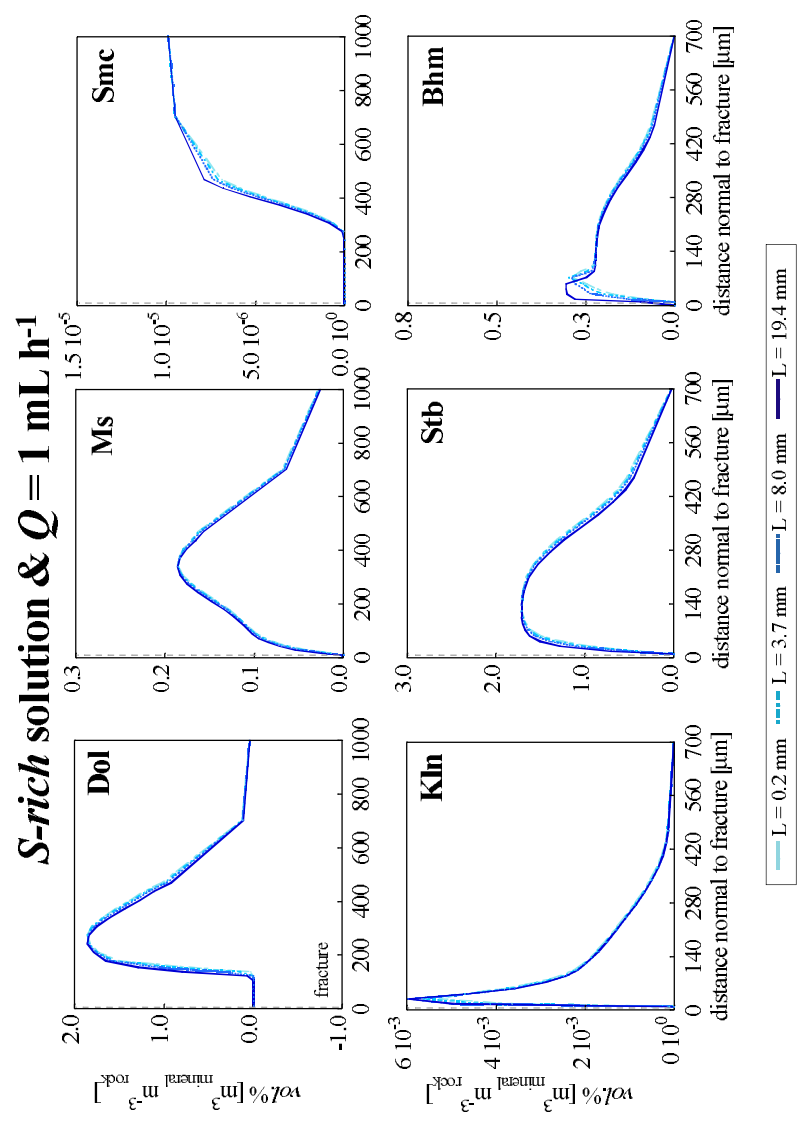


Figure 10

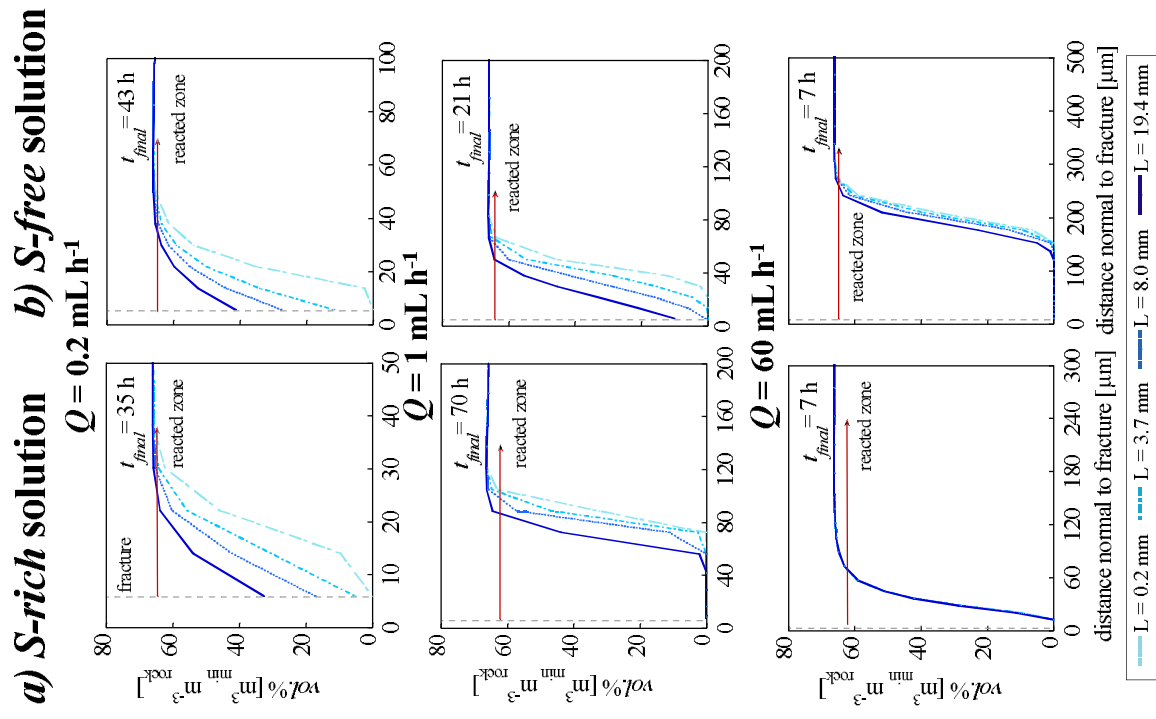


Figure 11

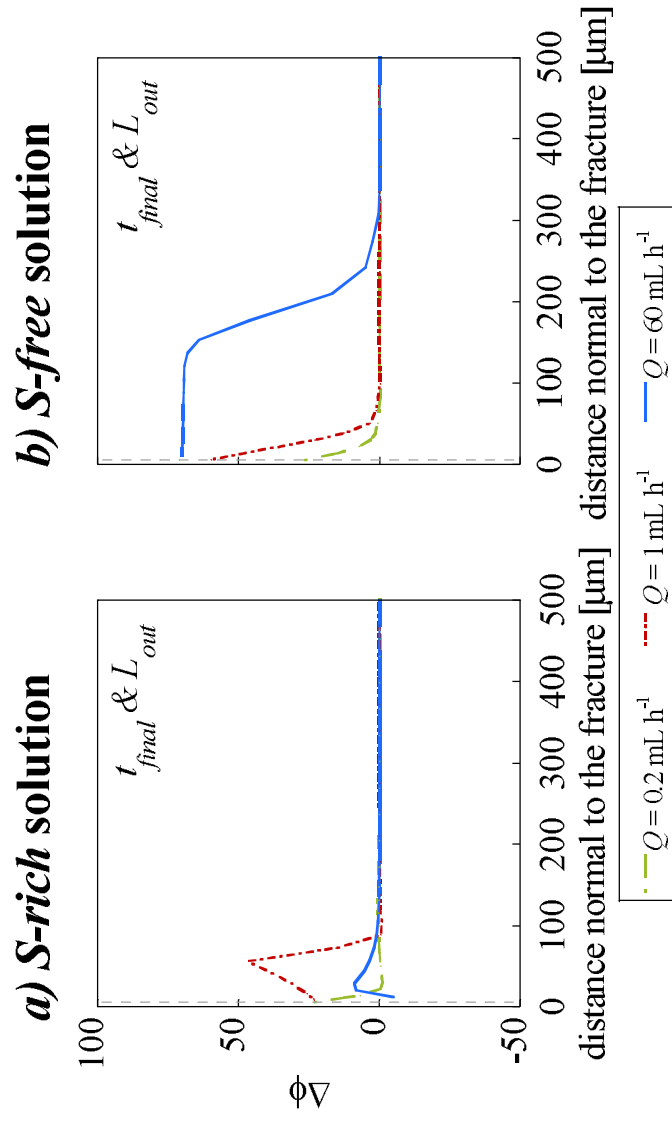


Figure 12

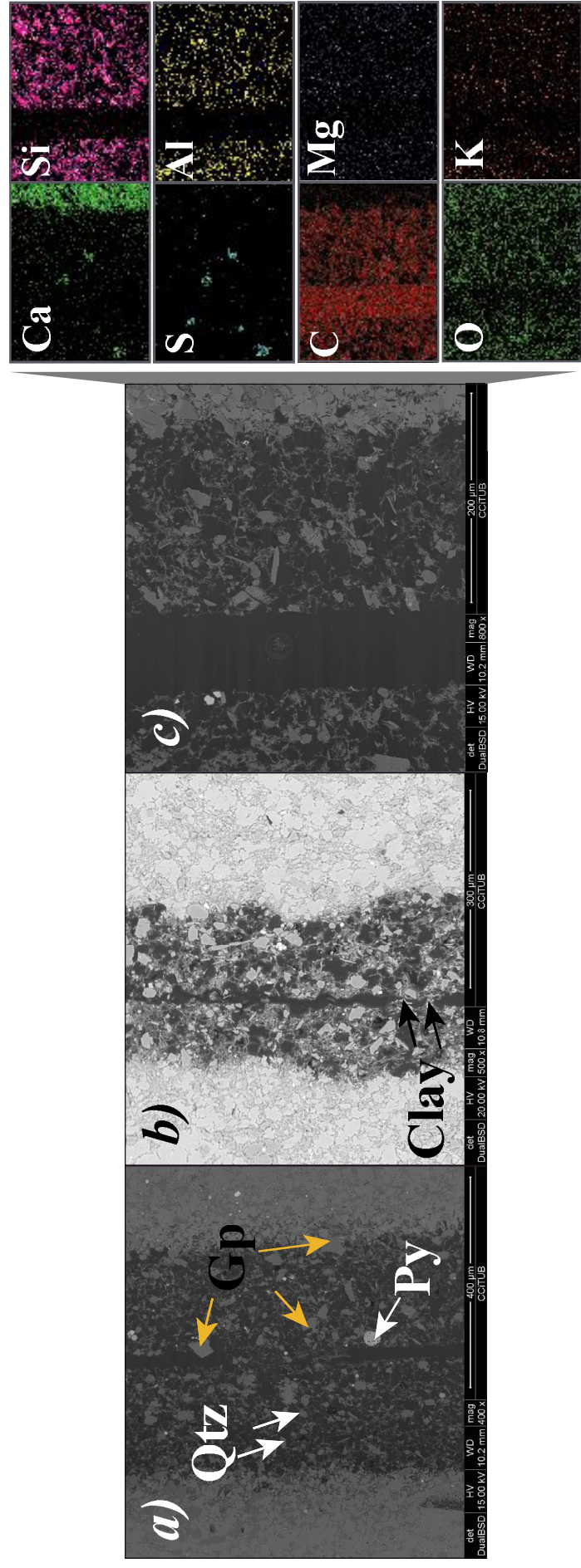
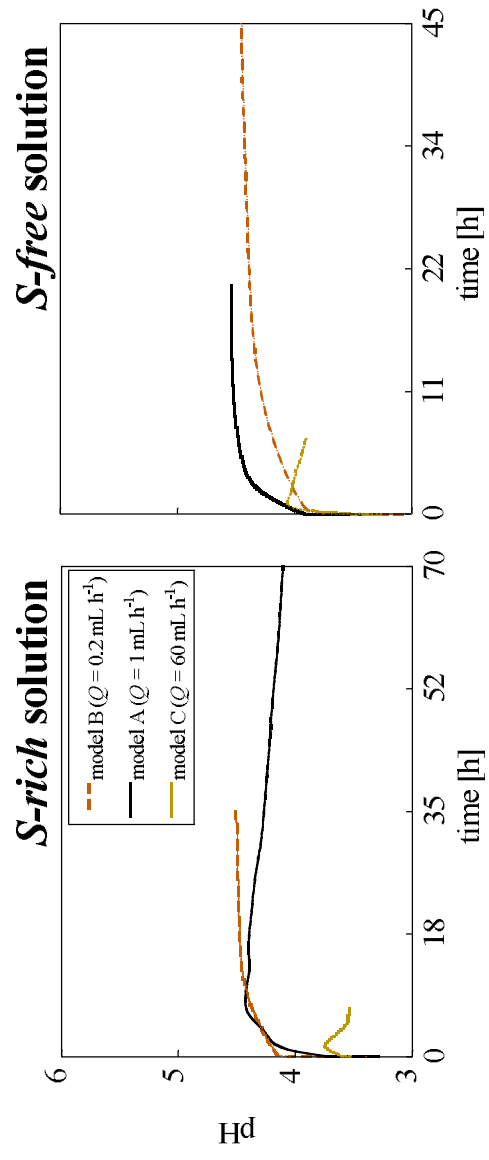


Figure B1



**Supplementary Material**

[Click here to download Supplementary Material: supplementary data-revised2.docx](#)

## Appendixes

[Click here to download Supplementary Material: Appendixes2.doc](#)